Shape coexistence in the near-spherical ^{142}Sm nucleus

S. Rajbanshi,[1] Abhijt Bisoi,[1] Somnath Nag,[2] S. Saha,[3] J. Sethi,[3] T. Trivedi,[3] T. Bhattacharjee,[4] S. Bhattacharyya,[4] S. Chattopadhyay,[1] G. Gangopadhyay,[5] G. Mukherjee,[4] R. Palit,[3] R. Raut,[6] M. Saha Sarkar,[1] A. K. Singh,[2] and A. Goswami[1,*]

[1]*Saha Institute of Nuclear Physics, 1/AF, Bidhannagar, Kolkata 700064, India*

[2]*Indian Institute of Technology, Kharagpur 721302, India*

[3]*Tata Institute of Fundamental Research, Mumbai 400005, India*

[4]*Variable Energy Cyclotron Center, Kolkata 700064, India*

[5]*Department of Physics, University of Calcutta, Kolkata 700009, India*

[6]*UGC-DAE Consortium for Scientific Research, Kolkata 700098, India*

(Received 26 November 2013; published 21 January 2014)

High spin states of ^{142}Sm have been investigated using the fusion-evaporation reaction ^{116}Cd (^{31}P, $p4n$) at beam energy 148 MeV using the Indian National Gamma Array (INGA). Approximately sixty new gamma transitions have been placed in the proposed level scheme, which has been extended up to ≈12.5 MeV. Several band-like structures including one dipole band and three quadrupole bands have been observed in the proposed level scheme. Lifetimes of several levels in the dipole band and quadrupole bands have been measured using doppler shift attenuation method (DSAM). The deduced $B(M1)$ values for the dipole band have been compared with the semiclassical shears mechanism with the principle axis cranking (SPAC) model, and the dipole band has been interpreted as a magnetic rotational band. Comparisons between the experimental characteristics and cranked Nilsson-Strutinsky (CNS) calculations for the observed quadrupole bands indicate that these bands have been formed on the triaxial deformed shape of ^{142}Sm.

DOI: 10.1103/PhysRevC.89.014315 PACS number(s): 21.10.Re, 21.10.Tg, 23.20.Lv, 27.60.+j

I. INTRODUCTION

Spectroscopic investigation of nuclei with neutron number below 82 shell closure has been rich in experimental findings as well as theoretical understanding of the various excitation mechanisms responsible for the generation of both low and high spin states in nuclei in this mass region. In the $A = 130$–150 region, a variety of minima corresponding to spherical or near-spherical, low-deformation oblate or prolate, triaxial, and superdeformed shapes have been observed in potential energy surface calculations [1]. It has been observed that, depending upon the availability of orbitals for protons and neutrons near the Fermi surface, the nuclear shapes can evolve as well as coexist with increasing excitation energy and spin.

The nuclei with $A \approx 140$ having a few holes in the $N = 82$ shell closure are spherical or only slightly deformed in the ground states [2]. They can be easily polarized by unpaired nucleons resulting from broken pairs available for the particular nucleus. For these nuclei there also exists a competition between the differing shape-driving effects of the protons and neutrons. The occupied $h_{11/2}$ proton orbits tend to favor prolate shapes with $\gamma = 0^\circ$ because they are in the low-omega oribtals of $h_{11/2}$. In contrast, the neutron configurations tend to favor oblate shapes with $\gamma = -60^\circ$ because the high-omega oribtals of $h_{11/2}$ neutron shell are occupied. Both the associated prolate and oblate potential-energy minima are predicted to have similar energies [3–5] which can drive the nuclear shape to triaxiality. At high spins the combined contribution of neutron holes and neutron particles in the high-j orbitals across the $N = 82$ gap as well as proton particles and holes across the $Z = 64$ semishell closure drives the nuclear shape toward a stable triaxial deformation with $\gamma = +30^\circ$ [1,6]. Moreover, due to the availability of particles and holes in the high j orbitals, such as $\pi h_{11/2}$ and $\nu h_{11/2}$, phenomena such as magnetic rotation would be expected as a possible mechanism for the generation of angular momentum. Indeed, several dipole bands, interpreted as magneticrotational (MR) bands [7–10], have been observed in this mass region, along with quadrupole bands based on triaxial shape with classically unfavored rotation around the longest principle axis [11].

Isotopes of Sm ($Z = 62$) in the vicinity of the ^{146}Gd ($Z = 64$, $N = 82$) core have been subjects of many spectroscopic investigations over the last two decades. In particular, several studies on the observation of dipole bands in Sm isotopes were reported in the literature [7,8,12–15], of which the ones in ^{139}Sm were interpreted as MR bands in the light of lifetime measurements [7,8] and theoretical calculations with the tilted axis cranking (TAC) [16,17] model. Further, quadrupole bands were observed in Gd isotopes [11,18,19] wherein lifetime measurements were carried out for $B(E2)$ values. Similar investigations in Sm isotopes are still not avilable.

The present work pertains to the in-beam gamma spectroscopy of the ^{142}Sm ($Z = 62$, $N = 80$) nucleus populated through a heavy-ion induced fusion-evaporation reaction. The nucleus was previously studied by Lach *et al.* [20] using (α, $4n$) and (^{3}He, $3n$) reactions, from which the level scheme was proposed up to an excitation energy of ≈6 MeV. The study also confirmed a 10^+ isomeric state at 3.662 MeV with $\tau = 480 \pm 60$ ns. The present investigation is primarily aimed at observation of MR bands in the ^{142}Sm nucleus with an additional motivation to probe for quadrupole bands and infer the associated shape evolution and/or coexistence.

*asimananda.goswami@saha.ac.in

II. EXPERIMENTAL DETAILS

High spin states of ^{142}Sm were populated by the reaction ^{116}Cd (^{31}P, $p4n$) at a beam energy of 148 MeV provided by the TIFR-BARC Pelletron Linac facility, Mumbai. An isotopically enriched (≈99%) ^{116}Cd target of thickness 2.4 mg/cm^2 was used. The backing was Pb of 14.5 mg/cm^2 thickness such that all residues were stopped in the target and/or backing combination. The recoil velocity of the compound nucleus was ≈2% of c. The nucleus ^{142}Sm was populated through the ($p4n$) channel which has about 30% of the total cross-section. The Indian National Gamma Array (INGA) at TIFR, Mumbai was used to detect the deexciting gamma rays produced in the reaction.

During the experiment INGA comprised nineteen Compton suppressed clover detectors arranged in six different angles, with four detectors at 90° and three each at 40°, 65°, 115°, 140°, and 157° with respect to the beam direction. The target-to-detector distance was 25 cm.

The digital data acquisition (DDAQ) system consisted of six Pixie-16 modules, developed by XIA LLC [21], each one of which was able to support four clover detectors, arranged in a single PCI/PXI crate. A 12-bit 100 MHz flash analog-to-digital converter (FADC) was used to digitized the preamplifer signal coming from crystals of respective clover detectors. The BGO signals from the anti-Compton shield of the respective clovers were used for vetoing the individual channels. A valid fast trigger was generated in the absence of the veto pulse in a specific time window. For a given channel, fast trigger validation was done and the time-stamped event header information was written. Detailed information about the DDAQ has been given in Ref. [22].

These time-stamped data from different Pixie modules were merged to a single data stream in ofline mode. The data sorting routine, multiparameter time-stamped based coincidence search program (MARCOS) [22], developed at the Tata Institute of Fundamental Research (TIFR), was used to sort the time-stamped combined data stream into usual coincident events based on the mapping of DDAQ channels to different crystals of the detectors in the array. The MARCOS program was used to find out energy calibration coefficients of each crystal and then perform gain matching between the different crystals of the clover detector. Setting the proper time window an as external parameter, the program MARCOS was used to find out the prompt gamma–prompt gamma and prompt gamma–delayed gamma correlations.

III. DATA ANALYSIS

The sorting program MARCOS was used to generate different symmetric and angle-dependent E_γ-E_γ matrices as well as a symmetric E_γ-E_γ-E_γ cube with a time window of 100 ns. The symmetric E_γ-E_γ matrix contained ≈4 × 10^9 two- and higher-fold gamma-gamma coincidence events. Relative efficiency and energy calibrations of the detection system (INGA) were performed with the radioactive sources ^{152}Eu and ^{133}Ba, placed at the target position of the array.

The level scheme of ^{142}Sm was constructed on the basis of the intensity measurement and coincidence relationship established from the symmetric E_γ-E_γ matrix and E_γ-E_γ-E_γ cube using the INGASORT [23] and RADWARE [24,25] software packages. The multipolarities and the electromagnetic characters of the observed gamma transitions, for assigning the spin-parities of the levels, were determined from analysis of the angle-dependent asymmetric matrices, as detailed subsequently in this section.

Preferential population of magnetic substates in heavy-ion reaction leads to an alignment which induces anisotropy in the angular distribution of gamma transitions [26,27]. The experimental angular distributions were analyzed in terms of the Legendre polynomial expression,

$$W(\theta) = A_0[1 + a_2 P_2(\cos\theta) + a_4 P_4(\cos\theta)],$$

where θ was the angle between detector and beam axis. The angular distribution coefficients a_2 and a_4 were obtained from the χ^2 minimization of $W(\theta)$ to the experimental yield at different angles.

An extensively used technique for multipolarity assignment of gamma transitions is through the determination of the ratio for directional correlation from oriented states (DCO), and the same was carried out in the present work. The DCO ratio [28,29] for a gamma transition (γ_1) at an angle θ_1 with respect to another transition (γ_2) at an angle θ_2 is defined as

$$R_{\rm DCO} = \frac{I_{\gamma_1}\ (\text{measured at } \theta_1;\ \text{gated by } \gamma_2 \text{ at } \theta_2)}{I_{\gamma_1}\ (\text{measured at } \theta_2;\ \text{gated by } \gamma_2 \text{ at } \theta_1)},$$

where I_{γ_1} is the intensity of γ_1 at an angle θ_1. In the present study, the detectors at $\theta_1 = 140°$ and $\theta_2 = 90°$ with respect to the beam direction were used to evaluate DCO ratios which were then compared with theoretical $R_{\rm DCO}$ ratios [30] for multipolarity and spin assignments. The theoretical $R_{\rm DCO}$ ratios were calculated using the software code ANGCOR [31]. Theoretically, for a stretched transition, the $R_{\rm DCO}$ ratio should be close to unity if the gate is on a transition with the same multipolarity. If the gating transition has a multipolarity different from the observed transition (γ_1) or the latter is a transition of mixed nature, then the $R_{\rm DCO}$ entirely depends on the detector angles (θ_1, θ_2), mixing ratio (δ), and the width of the substate population (σ/j) of the reaction. Theoretically, as far as present geometry is concerned, $R_{\rm DCO} \approx 1.9$ was obtained for a stretched quadrupole transition gated by a pure dipole transition. Similarly, the gate on a stretched quadrupole transition gave the $R_{\rm DCO}$ value ≈0.5 for a pure dipole transition. In this calculation, the width of the substate population (σ/j) was assumed to be 0.3. The $R_{\rm DCO}$ ratios for gamma transitions were obtained from an angle-dependent E_γ-E_γ matrix and corrected for the efficiency of the detectors, which were placed at two different angles θ_1 and θ_2. This efficiency correction was required as we were using the add-back spectrum to evaluate DCO ratios for which the effective number of crystals at different angle should be taken into account.

The $R_{\rm DCO}$ ratios for certain weak transitions could not be determined owing to their poor statistics. An alternative method by determining the angular distribution from oriented nuclei (ADO) ratio [32] was adopted for them. For this, two angle dependent matrices were constructed which stored the coincidence information between the detectors at 40° and 90°

and the rest of the detectors. The angular distribution ratio for a gamma transition (γ_1) can be expressed as

$$R_\theta = \frac{I_{\gamma_1}\text{ (measured at }\theta_1 = 40^\circ\text{; gated by all)}}{I_{\gamma_1}\text{ (measured at }\theta_2 = 90^\circ\text{; gated by all)}}.$$

Setting a gate on all detectors eliminates the effect of the gating transition on the measured ADO ratio. The values of R_θ, obtained for the stretched quadrupole and dipole transitions in ^{142,143}Eu [32], the other strongly populated nuclei in the present experiment, were 1.6 and 0.60, respectively. For the $\Delta I = 0$ dipole transition the value of R_θ was also found to be 1.60. Intermediate values of R_θ between these two values indicated their quadrupole/dipole mixed nature, and $R_\theta < 0.60$ was obtained for the transitions having negative admixture.

The use of a clover detector facilitates determination of linear polarization of the observed gamma transitions, thus aiding the identification of their electromagnetic character. The polarization information along with the multipolarity assignments from $R_{\rm DCO}/R_\theta$ measurements helps in concluding the spin-parities of the associated levels [33,34]. Polarization (P) of a gamma radiation depends on the polarization sensitivity (Q) and the polarization asymmetry (A) through the relation, $P = A/Q$. The polarization asymmetry of a Compton scattered photon has been defined as [33,35–37],

$$A = \frac{a(E_\gamma)N_\perp - N_\parallel}{a(E_\gamma)N_\perp + N_\parallel},$$

where $N_\parallel$ and $N_\perp$ denote the number of events scattered in parallel and perpendicular directions to the reaction plane, respectively. The asymmetry correction factor $a(E_\gamma)$ indicates the geometrical asymmetry in the detection system and was determined from

$$a(E_\gamma) = \frac{N_\parallel}{N_\perp},$$

using gamma-ray transitions from an unpolarized radioactive source. We evaluated the asymmetry correction factor $a(E_\gamma)$ as a function of energy using the radioactive ^{152}Eu and ^{133}Ba sources. The factor was observed to remain at an almost constant value 0.98 over an energy range from 300 to 1400 keV (Fig. 1).

The experimental asymmetry, A, for the transitions of interest, was evaluated from the two E_γ-E_γ matrices. One matrix contained events in which one of the gamma rays was scattered inside the clover detector placed at 90° with respect to the beam axis, in the direction perpendicular to the emission plane, while a coincident gamma ray was registered in any clover placed at the other angles. The other matrix was almost similar, except for the fact that the gamma rays were scattered inside the clover, in the direction parallel to the emission plane.

The polarization sensitivities at different gamma-ray energies were determined using strong transitions from different residual nuclei populated in the present reaction. The experimental asymmetries (A) for these transitions were determined using the above technique. The linear polarizations (P) were calculated (Table I) using the Klein-Nishina formula [38] with the angular distribution coefficients obtained either from

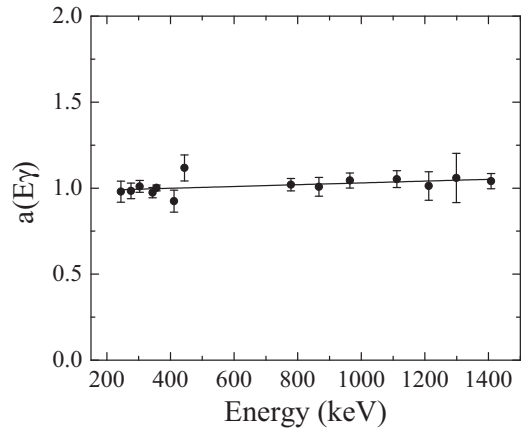

FIG. 1. The asymmetry correction factor $a(E_\gamma)$ for the clover detector placed at 90° with respect to the beam direction. The solid line shows a linear fit of the data points.

analysis of the singles data in the present experiment or from values available in the literature [39,40]. The resulting polarization sensitivities were fitted (Fig. 2) using the function [33,35–37]

$$Q(E_\gamma) = Q_0(a + b \times E_\gamma),$$

where Q_0 is called the polarization sensitivity for the ideal Compton polarimeter and is defined as

$$Q_0 = \frac{(1+\alpha)}{(1+\alpha+\alpha^2)} \quad \text{with } \alpha = \frac{E_\gamma\text{ (keV)}}{511}.$$

Least-squares fitting of experimental polarization sensitivity $Q(E_\gamma)$ gave $a = 0.74(0.10)$ and $b = 3.5(1.1) \times 10^{-4}$ in keV^{-1}. A positive value of linear polarization (P) is indicative of electric character whereas a negative value indicates magnetic character of the transitions. The linear polarization for a mixed transition was expected to be close to zero.

IV. EXPERIMENTAL RESULTS

The proposed partial level scheme of ^{142}Sm, obtained from the present experiment (Fig. 3), was established using the coincidence relationship, relative intensity, $R_{\rm DCO}$, R_θ,

TABLE I. Experimental asymmetry (A), polarization (P) and polarization sensitivity (Q) for gamma rays produced in the present experiment. Angular distribution coefficients a_2 and a_4 were taken from Refs. [39] and [40] for ^{141}Eu and ^{143}Eu respectively.

Nucleus	E_γ (keV)	A	P	Q
^{141}Eu	526.1	+0.25(0.02)	+0.52(0.17)	0.48(0.16)
^{141}Eu	722.3	+0.18(0.01)	+0.44(0.17)	0.41(0.16)
^{141}Eu	832.0	+0.16(0.01)	+0.48(0.18)	0.34(0.13)
^{141}Eu	846.9	+0.13(0.01)	+0.38(0.14)	0.34(0.13)
^{141}Eu	898.9	+0.13(0.02)	+0.66(0.33)	0.20(0.10)
^{143}Eu	916.4	+0.13(0.01)	+0.54(0.05)	0.25(0.03)
^{141}Eu	1279.9	+0.03(0.01)	+0.14(0.08)	0.18(0.11)

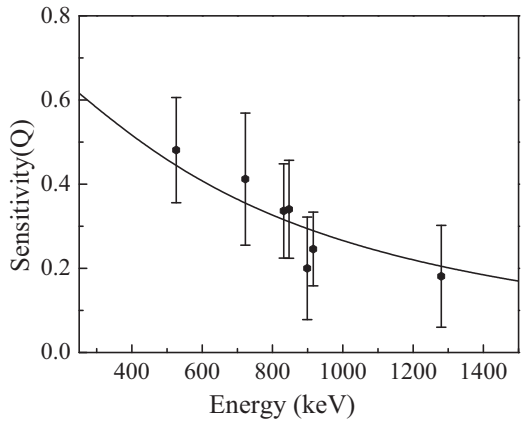

FIG. 2. The measured Polarization sensitivity of the clover detector. The solid line is the fitted curve of the experimental data points.

and linear polarization measurements. The intensities of the observed gamma transitions above the 7^- state were measured from singles as well as the gated spectrum and normalized with the 741.1 keV ($8^- \rightarrow 7^-$) gamma transition. For DCO ratios measurement 907.2 and 919.9 keV quadrupole transitions were used as gating transitions. The level scheme was extended up to an excitation energy $\approx$12.5 MeV and spin of $28\hbar$. A total of 63 new gamma transitions were placed in the proposed level scheme, which shows a very complex and irregular structure at low spin. The gamma energies, relative intensities, $R_{\rm DCO}$, R_θ, linear polarizations (P) and assigned spin-parities of the relevant levels of ^{142}Sm are given in Table II.

All the previously observed gamma transitions by Lach *et al.* [20] and Kennedy *et al.* [41] were observed in the present experiment. We measured the angular distribution of some of the previously reported strong, uncontaminated transitions, viz., 273.8, 919.9, and 907.2 keV (Fig. 4). From the evaluated a_2 and a_4 coefficients, it was concluded that the 273.8 keV transition has a pure dipole character whereas the 919.9 and 907.2 keV transitions are pure quadrupole transitions. This assignment agrees with the previous work [20] and justifies the use of the 907.2 and 919.9 keV transitions as the gating transition for subsequent DCO ratio measurements.

The $R_{\rm DCO}$ and linear polarization (P) values of the 677.1 keV transition confirmed its $M1/E2$ mixed nature, leading us to assign a spin-parity of 14^- to the state which depopulates through 677.1 and 90.5 keV transitions. Measured R_θ and $R_{\rm DCO}$ ratios of the 715.6, 506.7, 387.5, 90.5, and 85.6 keV transitions were well in agreement with the previously assigned dipole character of these transitions. Linear polarization measurements of the 506.7 and 387.5 keV transitions showed their mixed $M1/E2$ nature. We have assigned to the states which depopulate via the 506.7 and 387.5 keV transitions, respectively, spin-parity values of 12^+ and 13^+. This assignment required the 302.3 keV transition to be a $\Delta I = 0$ and 90.5 keV transition to be an $E1$ transition, respectively. The $R_{\rm DCO}$ and R_θ measurements of the former agreed with the $\Delta I = 0$ assignment.

A sequence of stretched $E2$ transitions was observed above the 10^+ state which depopulated through the 438.9 keV transition. This sequence was extended up to the level having spin-parity 18^+. Several new transitions (428.0, 686.0, 727.1, 908.0, 951.8, 982.0, 1066.0, 1280.5, and 1324.4 keV) were observed between these two excited states as shown in the sum of the double-gated spectra with gates on 438.9, 919.9, 428.0, and 578.8 keV transitions [Fig. 5 (a)]. The R_θ and $R_{\rm DCO}$ ratio measurements showed all these to be quadrupole transitions. Linear polarizations of the 951.8, 1280.5, and 428.0 keV transitions confirmed their $E2$ character. We assigned the spin-parities of the states which depopulate through the 951.8, 1280.5, and 428.0 keV transitions as 14^+, 16^+, and 18^+, respectively. Several parallel cascades were observed between the levels having spin 12^+ and 18^+. Above the 18^+ level the level scheme is fragmented into three structures, labeled as I, II, and III in Fig. 3.

A. Structure I

Above the 18^+ level, a cascade consisting of the 578.8, 840.0, 1078.0, 1249.0, and 1406.0 keV transitions, was observed [Fig. 5 (b)]. Measured $R_{\rm DCO}$, R_θ, and linear polarization values for the 578.8, 840.0, and 1078.0 keV transitions allowed us to interpret them as stretched $E2$ transitions. Due to the weak nature of the 1249.0 and 1406.0 keV transitions, we could not measure their $R_{\rm DCO}$ and linear polarization values. However, measured values of R_θ for these two transitions, 1.64(0.26) and 1.43(0.21), respectively, justifiies identifying them as stretched $E2$ transitions.

B. Structures II and III

We observed two more cascade-like structures consisting of the 634.5, 817.3, and 1040.0 keV transitions (structure II) and the 544.0, 557.9, 815.0, 923.8, and 973.0 keV transitions (structure III) populating the 22^+ and 20^+ levels of structure I, respectively [Figs. 3, 5(b), and 5(c)]. The R_θ, $R_{\rm DCO}$, and linear polarization measurements for the 634.5 keV (structure II) transition showed its $M1/E2$ character, whereas those for the 557.9, 815.0 and 923.8 keV (structure III) transitions confirmed their electric quadrupole nature. Owing to the weak nature of the 973.0 (structure III), 1040.0, and 817.3 keV (structure II) transitions, it was not possible to find out the linear polarization. However, $R_{\rm DCO}$ and R_θ values were in good agreement with their quadrupole nature. The R_θ and $R_{\rm DCO}$ values for the 544.0 keV (structure III) transition showed its $\Delta I = 1$ nature. The polarization measurement for the 544.0 keV transition was very crucial because the parity of structure III depends on the electromagnetic character of the 544.0 keV transition. The linear polarization measurement for the 544.0 keV transition from 578.8 and 428.0 keV gated spectra gave a high positive value but with large uncertainty [+0.34(0.16)]. On the other hand, it gave a value close to zero when measured from the 919.9 and 438.9 keV gated spectra. Hence, the state of linear polarization for the 544.0 keV transition could not be firmly identified from the present experimental investigation. We tentatively assigned the 544.0 keV transition $E1$ character. The parity of the state, connected through the 557.9 keV transition, as well as the parity of structure III remained uncertain.

TABLE II. Energy (E_γ), relative intensity (I_γ), $R_{\rm DCO}$, R_θ, linear polarization (P), and assignment of the gamma transitions for ^{142}Sm.

Energy (E_γ)	Intensity (I_γ)	J_i^π	J_f^π	DCO ratio ($R_{\rm DCO}$)	Anisotropy (R_θ)	Polarization (P)	Assignment
69.0		(14^-)	13^-				
75.0		$16^{(-)}$	15^-	0.72(0.06)[a]	1.18(0.16)		$(M1/E2)$
78.0		12^+	11		1.05(0.15)		$(M1/E2)$
85.6	20.0(17)	13^+	12^+	0.59(0.05)[a]	0.85(0.09)		$M1$
90.5	7.8(5)	14^-	13^+	0.62(0.08)[a]	0.88(0.13)		$E1$
163.9		10^+	10^+		1.63(0.11)		$M1$
174.9	16.0(3)	13^-	11^-		1.78(0.19)		$E2$
183.7	7.7(8)	20	19		0.77(0.09)		$(M1)$
189.4	9.2(6)	19	18	0.75(0.05)[a]	0.94(0.12)		$(M1/E2)$
193.8	50.0(2)	15^-	14^-	0.64(0.02)[a]	0.89(0.10)	−0.11(0.08)	$M1/E2$
201.1	58.0(1)	8^-	7^-		0.68(0.12)	−0.25(0.10)	$M1$
215.8	3.0(6)	17^-	16^-	1.05(0.13)[b]	0.69(0.10)		$M1$
237.2	4.0(7)	21	20		1.11(0.17)		$(M1/E2)$
245.0	2.2(13)	$14^{(-)}$	13^-	0.74(0.22)[a]	0.79(0.17)		$(M1/E2)$
252.9	74.6(1)	13^-	11^-	2.04(0.05)[b]	1.65(0.10)	+0.43(0.18)	$E2$
254.0	11.0(7)	18	17		0.80(0.15)		$(M1/E2)$
264.9	12.2(4)	14^-	13^-	0.65(0.03)[a]	0.77(0.09)	−0.16(0.09)	$M1/E2$
270.0	4.6(12)	17	16	0.57(0.07)[a]	0.70(0.14)		$(M1)$
273.8	134(4)	9^-	8^-		0.61(0.09)		$M1$
274.9	12.8(5)	10^+	9^-	0.95(0.08)[b]	1.02(0.16)	+0.27(0.09)	$E1$
277.1	3.4(11)	20^-	19^-	1.12(0.08)[b]	0.89(0.21)	−0.04(0.08)	$M1/E2$
286.7	14.0(4)	17^-	16^-	1.06(0.04)[b]	0.54(0.07)	−0.37(0.15)	$M1$
299.1	1.1(18)	16^+	16^+		1.72(0.43)		$M1$
302.3	7.0(7)	12^+	12^+	1.46(0.15)[b]	1.78(0.15)		$M1$
310.0	3.8(12)	18	17	0.61(0.06)[a]	0.56(0.08)		$(M1)$
319.4	9.5(5)	11^-	10^-	1.08(0.09)[b]	0.81(0.10)	−0.05(0.10)	$M1/E2$
336.0		10^+	8^+				$E2$
345.6	18.2(3)	16^-	15^-	0.67(0.06)[a]	0.79(0.09)	−0.03(0.05)	$M1/E2$
351.8	30(2)[c]	17^+	16^+	0.47(0.02)[a],[d]	0.60(0.10)	−0.25(0.10)	$M1$
352.0		(22)	(21)		0.78(0.12)		$(M1/E2)$
372.2	0.8(21)	23^+	$23^{(-)}$				
385.2	15.0(5)	18^-	17^-	0.89(0.05)[b]	0.56(0.09)	−0.32(0.12)	$M1$
387.5	6.7(7)	13^+	12^+	0.97(0.10)[b]	0.85(0.10)	−0.29(0.16)	$M1$
397.1	4.0(19)	11^-	10^-	1.09(0.09)[b]	0.65(0.14)	−0.45(0.20)	$M1$
408.0	5.0(8)	21^-	20^-	0.89(0.06)[b]	0.57(0.11)	−0.33(0.15)	$M1$
428.0	15.2(3)	18^+	16^+	0.97(0.07)[a]	1.55(0.12)	+0.40(0.17)	$E2$
438.9	42.2(3)	10^+	9^-	1.14(0.09)[b]	0.85(0.08)	+0.33(0.12)	$E1$
474.3	11.1(2)	9^-	7^-		1.32(0.19)	+0.30(0.18)	$E2$
491.8		7^-	6^+				$E1$
499.6	8.2(12)	19^-	18^-	0.91(0.04)[b]	0.53(0.08)	−0.45(0.18)	$M1$
506.7	2.6(8)	$22^{(-)}$	21^-	0.61(0.07)[a]	0.57(0.07)		$(M1)$
506.7	8.4(6)	12^+	11^+	0.86(0.06)[b]	0.57(0.08)	−0.02(0.01)	$M1/E2$
518.5	5.0(7)	16^-	15^-	1.21(0.10)[b]	0.69(0.09)	+0.09(0.13)	$M1/E2$
524.5	1.7(12)	(22)	(21)		0.73(0.19)		$(M1/E2)$
539.9	65.3(1)	7^-	7^-		1.56(0.18)		$M1$
543.3	10.8(3)	16^+	16^-		1.46(0.21)	+0.29(0.17)	$E1$
544.0	9.2(6)	$21^{(-)}$	20^+	0.66(0.06)[a]	0.91(0.16)	+0.34(0.16)	$(E1)$
556.5		5^-	4^+				$E1$
557.9	9.8(5)	$23^{(-)}$	$21^{(-)}$	0.93(0.11)[a]	1.60(0.19)	+0.29(0.14)	$E2$
563.7		5^-	3^-				$E2$
578.8	23.0(5)	20^+	18^+	0.96(0.11)[a]	1.47(0.21)	+0.45(0.19)	$E2$
587.5	10.1(4)	10^-	9^-	0.91(0.10)[b]	0.64(0.12)	−0.23(0.13)	$M1$
621.4	4.3(6)	20^-	19^-	0.88(0.11)[b]	0.54(0.10)	−0.35(0.21)	$M1$
628.6		6^+	4^+				$E2$
631.9		(4^-)	3^-				
634.5	5.3(6)	23^+	22^+	0.67(0.06)[a]	0.75(0.11)	−0.17(0.21)	$M1/E2$
677.1	43.5(2)	14^-	13^-	0.62(0.07)[a]	0.84(0.12)	+0.16(0.10)	$M1/E2$

TABLE II. (*Continued.*)

Energy (E_γ)	Intensity (I_γ)	J_i^π	J_f^π	DCO ratio ($R_{\rm DCO}$)	Anisotropy (R_θ)	Polarization (P)	Assignment
686.0	2.3(9)	18^+	$16^{(+)}$	0.93(0.12)[a]	1.59(0.17)	+0.32(0.14)	$E2$
715.6	9.0(2)	11^+	10^+	1.21(0.12)[b]	0.71(0.09)	−0.06(0.03)	$M1/E2$
727.1	3.4(12)	18^+	16^+	1.04(0.11)[a]	1.69(0.16)	+0.84(0.36)	$E2$
741.1	100.0(2)	8^-	7^-		0.53(0.09)		$M1$
767.9		2^+	0^+				$E2$
814.0	2.5(8)						
815.0	6.4(6)	$25^{(-)}$	$23^{(-)}$	0.89(0.15)[a]	1.45(0.12)	+0.40(0.17)	$E2$
817.3	3.7(10)	$25^{(+)}$	23^+	0.87(0.18)[a]	1.67(0.19)		$(E2)$
840.0	12.8(6)	22^+	20^+	1.04(0.05)[a]	1.45(0.18)	+0.56(0.23)	$E2$
844.3	6.6(10)	19^-	18^-	1.13(0.08)[b]	0.78(0.13)	−0.21(0.14)	$M1$
859.8	4.6(9)	(21)	20				
861.6	14.0(2)	10^-	8^-		1.47(0.26)	+0.38(0.26)	$E2$
906.0		8^+	6^+				$E2$
907.2	70.1(1)	11^-	9^-	1.98(0.05)[b]	1.62(0.15)	+0.50(0.20)	$E2$
908.0	4.9(12)	14^+	12^+	0.99(0.06)[a]	1.84(0.25)	+0.48(0.20)	$E2$
911.0					1.24(0.23)	+0.09(0.14)	$(M1/E2)$
919.9	25.0(2)	12^+	10^+	2.00(0.10)[b]	1.46(0.21)	+0.48(0.13)	$E2$
923.8	4.3(6)	$27^{(-)}$	$25^{(-)}$	0.88(0.09)[a]	1.47(0.25)	+0.32(0.14)	$E2$
946.6	2.0(12)	18^+	16^-	1.87(0.29)[b]	1.81(0.33)		M2
951.8	6.8(5)	14^+	12^+	0.95(0.07)[a]	1.56(0.17)	+0.47(0.22)	$E2$
954.0		8^+	7^-				$E1$
973.0	1.8(24)	$29^{(-)}$	$27^{(-)}$	0.85(0.11)[a]	1.40(0.29)		$(E2)$
982.0	2.2(6)	16^+	14^+		1.42(0.21)	+0.74(0.32)	$E2$
984.9	15.0(2)	11^-	9^-	2.07(0.16)[b]	1.78(0.26)	+0.58(0.27)	$E2$
1023.2		4^+	2^+				$E2$
1040.0	1.1(13)	$27^{(+)}$	$25^{(+)}$	1.01(0.13)[a]	1.41(0.20)		$(E2)$
1042.2	16.2(9)	16^-	15^-	0.52(0.05)[a]	0.60(0.11)	−0.51(0.23)	$M1$
1066.0	1.1(15)	$16^{(+)}$	14^+		1.75(0.27)		$(E2)$
1078.0	3.4(11)	24^+	22^+	1.16(0.13)[a]	1.71(0.19)	+0.62(0.26)	$E2$
1113.1	3.3(5)	$16^{(-)}$	15^-	1.20(0.16)[b]	0.67(0.12)		$(M1/E2)$
1212.1		(6^+)	4^+				
1222.1	3.6(3)	12^+	10^+	1.65(0.23)[b]	1.55(0.21)	+0.43(0.20)	$E2$
1249.0	1.5(9)	$26^{(+)}$	24^+		1.64(0.26)		$(E2)$
1280.5	4.9(3)	16^+	14^+	1.02(0.09)[a]	1.78(0.16)	+0.74(0.32)	$E2$
1290.3		10^-	7^-				$E3$
1303.2	1.0(18)	$16^{(+)}$	15^-				$(E1)$
1308.4		11	10^+		0.78(0.13)		$(M1)$
1324.4	2.5(6)	16^+	14^+	1.96(0.23)[b]	1.74(0.20)		$E2$
1342.0			5^-				
1406.0	1.0(10)	$28^{(+)}$	$26^{(+)}$		1.43(0.26)		$(E2)$
1486.1	1.6(15)	16^+	$16^{(-)}$				
1495.1	12.5(3)	16^+	14^-	0.90(0.06)[a]	1.45(0.12)	−0.46(0.26)	$M2$
1514.9	2.4(5)	16^+	$14^{(-)}$	1.01(0.16)[a]	1.43(0.28)		$(M2)$
1690.6	2.5(6)	16^+	(14^-)	1.16(0.21)[a]	1.49(0.31)		$(M2)$

Uncertainty in gamma-ray energy is ± (0.1–0.3) keV.
Intensities of gamma rays above the 7^- state are normalized to the 741.1 keV transition, with $I_\gamma = 100.0(2)$.
Intensity uncertainties does not include the errors due the uncertainty in efficiency correction.
[a]DCO ratios are obtained from the stretched quadrupole ($E2$) transition.
[b]DCO ratios are obtained from the pure stretched dipole ($M1$) transition.
[c]Intensity for the composite peak of 351.8 and 352.0 keV.
[d]DCO ratio is deduced for the unresolved doublet (351.8 + 352.0 keV).

In E_γ-E_γ-E_γ cube analysis a weak 372.2 keV transition was observed connecting the 23^+ state of structure II to the $23^{(-)}$ state of structure III. A few transitions, of energies 442.0, 262.0, and 1022.0 keV, were also observed in the coincidence spectra but could not be placed in the proposed level scheme of ^{142}Sm because of their weak intensities.

Two additional band-like structures were observed above the 252.9–677.1–193.8 keV cascade, as illustrated in Fig. 3. These structures are discussed below.

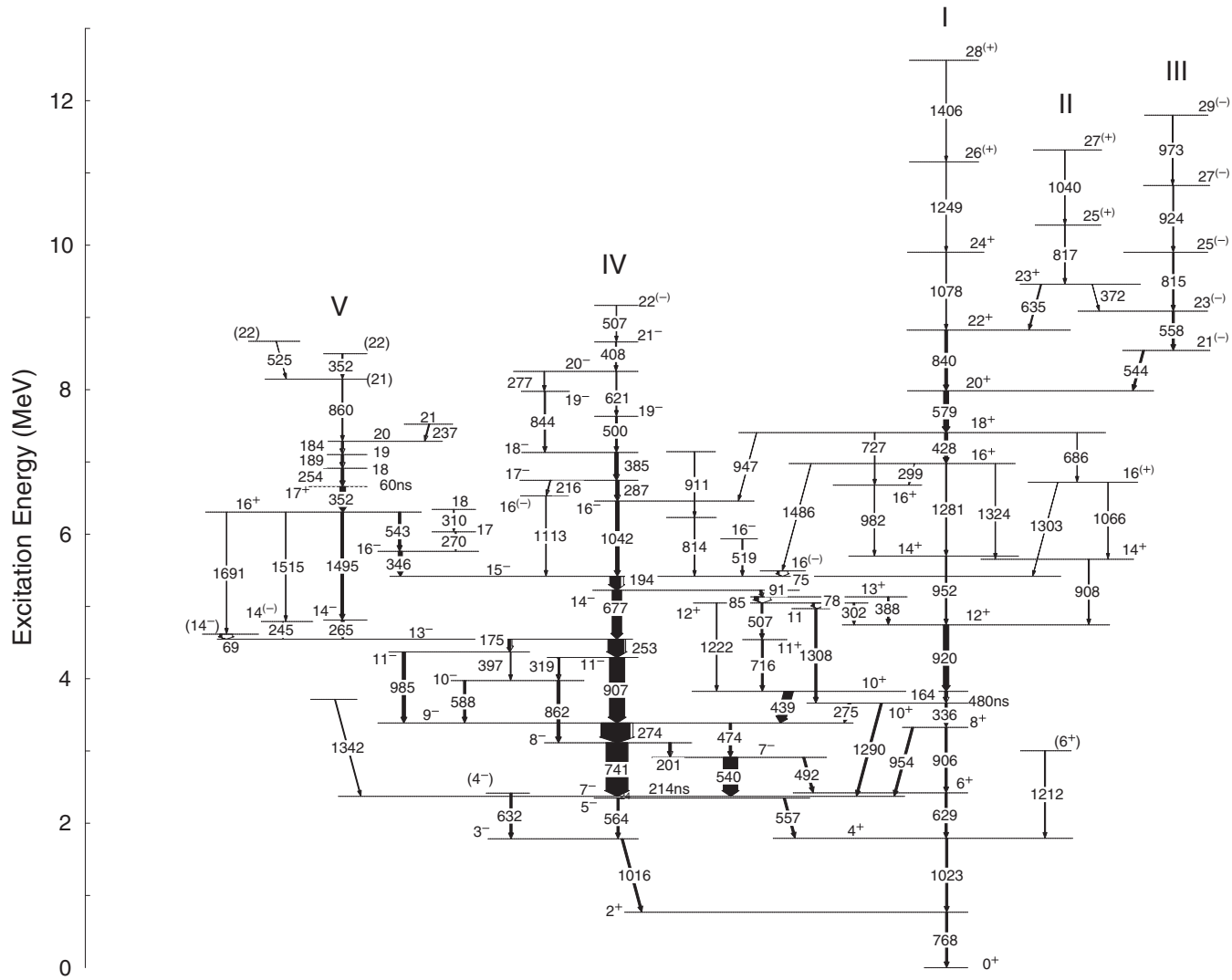

FIG. 3. The proposed level scheme of ^{142}Sm obtained from the present work. Transition energies are given in keV and widths of the arrows are proportional to the intensities of transitions. The energies are rounded off to keV.

C. Structure IV

In coincidence with the 193.8 and 1042.2 keV transitions a band-like structure, consisting of gamma rays of energies 286.7, 385.2, 499.6, 621.4, 408.0, and 506.7 keV, was observed, extending the level scheme up to the $22^{(-)}$ state. In the earlier work [20] a 385.2 keV transition was placed in between the 193.8 and 286.7 keV transitions. In the present experiment a new sequence of 1113.1 and 215.8 keV transitions was observed in coincidence with the 193.8, 677.1, 385.2, and higher lying transitions [Fig. 6(b)] but not in the spectrum gated by the 1042.2 and 286.7 keV transitions as shown in Fig. 6(a).

In this light the previous placement of the 286.7 and 385.2 keV transitions was changed with the 1042.2 and 286.7 keV transitions and placed in parallel to the 1113.1 and 215.8 keV transitions. We placed the 1042.2 keV transition just above the 193.8 keV transition on the basis of intensity measurement. Similarly, a cascade of 844.3 and 277.1 keV transitions was placed in parallel to the 499.6 and 621.4 keV transitions, as these transitions were absent in the spectra with gates on 499.6 and 621.4 keV transitions. The $R_{\rm DCO}$, R_θ, and linear polarization measurements for the 1042.2, 286.7, 385.2, 499.6, 621.4, 408.0, 506.7, and 844.1 keV transitions showed their $M1$ character. We have also observed two new $M1/E2$ mixed transitions of energies of 270.0 and 310.0 keV in coincidence with 345.6 and 193.8 keV transitions.

D. Structure V

Above the 13^- state, populated by the 677.1 keV transition, three parallel cascades were observed. The intensities of the 264.9 and the 1495.1 keV transitions were almost equal and we have placed the former below the latter. The spin-parity measurements of the corresponding states point towards a mixed nature for the 264.9 keV transition. The $R_{\rm DCO}$, R_θ, and polarization values for the 1495.1 keV transition were 0.90, 1.45, and -0.456, respectively, identifying it as an $M2$ transition. Hence, the spin-parity of the state which deexcities through it has been proposed to be 16^+. The $M2$ character of

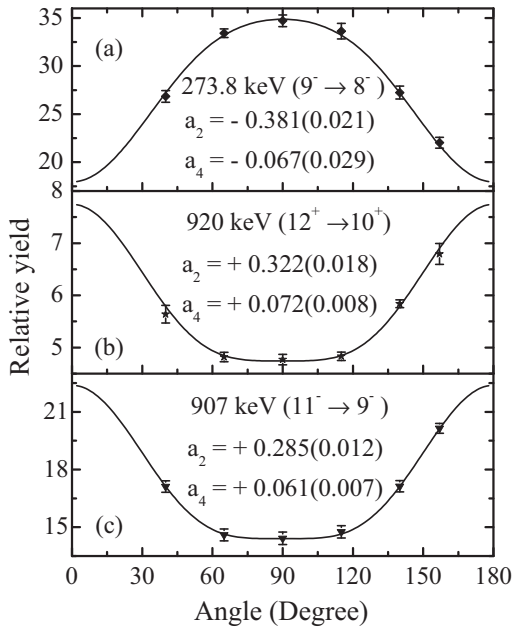

FIG. 4. Angular distribution of (a) 273.8 keV ($9^- \rightarrow 8^-$), (b) 919.9 keV ($12^+ \rightarrow 10^+$), and (c) 907.2 keV ($11^- \rightarrow 9^-$) transitions in ^{142}Sm. Solid lines represent the fits to the data points.

the 1495.1 keV transition would imply a Weisskopf estimate of 98 ps for this state.

In all the three parallel cascades, we observed a strong 351.8 keV transition whose intensity was greater than the sum of the intensities of these three parallel cascades. Accordingly, we could have placed this transition below these cascades. However, the double-gated spectrum of 345.6, 193.8, and 677.1 keV transitions also showed a 351.8 keV transition [Fig. 7 (b)]. Hence, we placed the 351.8 keV transition above the 16^+ states. This placement required a $\Delta I = 0$, $E1$ connection between the 16^+ and the 16^- states. The double-gated spectrum of the 351.8, 345.6, 193.8, and 677.1 keV transitions showed a peak at 543.3 keV which fitted the energy gap between the 16^+ and 16^- excited states. The multipolarity of 543.3 keV transition was confirmed as $\Delta I = 0$, $E1$ from R_θ and linear polarization measurements.

A new sequence of 254.0, 189.4, 183.7, 859.8, 237.2, and 524.5 keV transitions was observed [Fig. 7 (a)] above the 17^+ state which deexcited through the 351.8 keV dipole transition. The R_θ measurement for the 254.0, 183.7, 189.4, 237.2, and 524.5 keV transitions showed them to be $M1/E2$ in character. Owing to their weak nature, we were unable to extract any information about the linear polarization of these transitions and the parity of these states remains unknown. A 352.0 keV transition exists in the double-gated spectrum created by the 351.8 keV ($17^+ \rightarrow 16^+$) transition and all

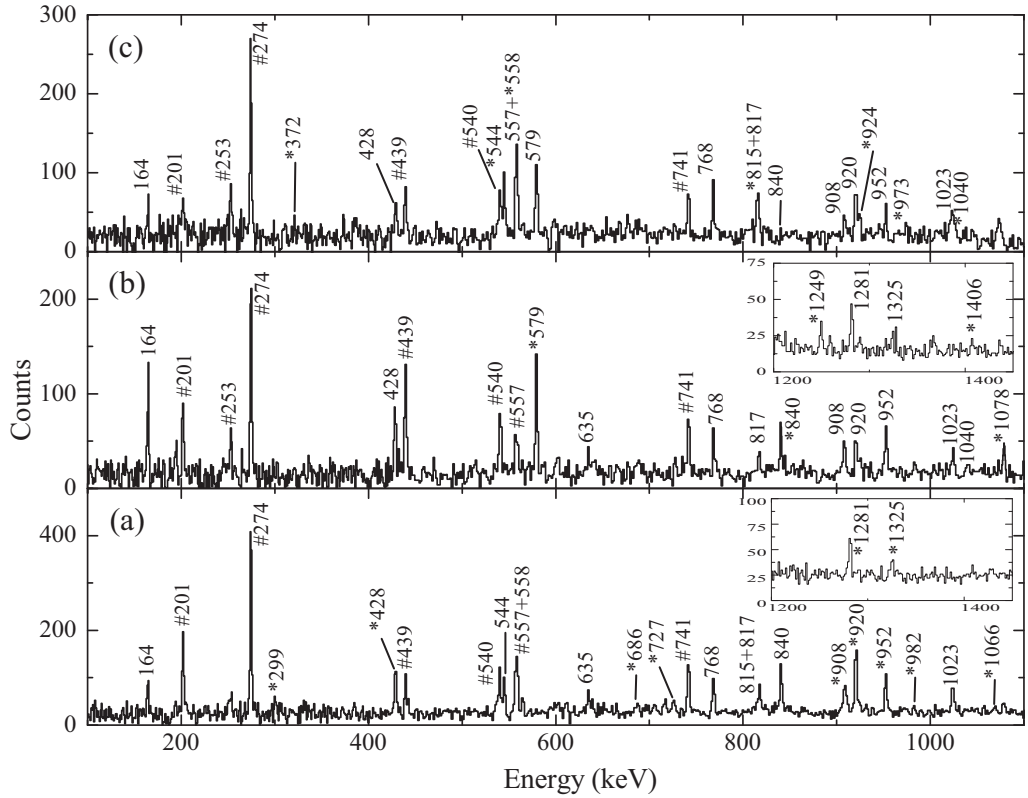

FIG. 5. Representative summed double-gated gamma-ray coincidence spectra show the transitions belonging to the positive parity states in ^{142}Sm. The peaks marked with hashes are previously assigned transitions in ^{142}Sm. The spectra were created with the sum of double-gated spectra of (a) 438.9, 919.9, 428.0, and 578.8; (b) 919.9, 428.0, 578.8, 840.0, and 1078.0; and (c) 428.0, 815.0, 557.9, 578.8, and 544.0 keV transitions. Peaks marked with asterisks are (a) the transitions between the states 10^+ and 18^+, (b) the transitions in structure I, and (c) the members of the structures II and III in ^{142}Sm.

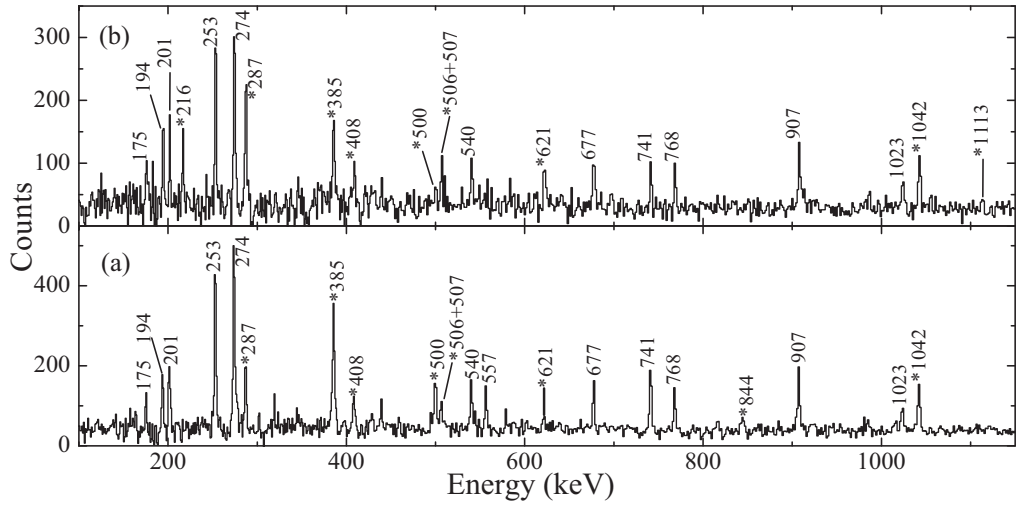

FIG. 6. Representative summed double-gated gamma-ray spectra, created by (a) 677.1, 193.8, 1042.2, and 286.7 and (b) 677.1, 193.8, 499.6, and 621.4 keV transitions, show the gamma rays between the negative parity states in ^{142}Sm. The peaks marked with asterisks are the members of dipole band-like structure IV in ^{142}Sm.

transitions of this sequence except the 524.5 and 237.2 keV transitions. We were not able to resolve this 352.0 keV transition from the strong 351.8 keV ($17^+ \rightarrow 16^+$) transition as they were in coincidence with each other. Hence, its intensity and electromagnetic nature remained unevaluated. Tentatively, the second 352.0 keV transition was placed at the top of this sequence.

We determined the mean life of the previously known 7^- isomeric state at 2372 keV by fitting an exponential decay to the time difference spectrum. This was constructed using the 741.1 keV transition above the 7^- state as "start" and any one of the transitions 556.5, 1023.2, and 767.9 keV was used as "stop". These three time-difference spectra were constructed from the time-stamped list-mode data as described by Palit *et al*. [22]. From the sum of these three time-difference spectra (Fig. 8), a mean life of 205(4) ns was extracted for the 7^- isomeric state. This was previously measured by Kennedy *et al*. [41] as 170 ± 2 ns using β-γ delayed coincidence.

We observed an intensity mismatch between the transitions populating the 17^+ state of structure V and deexciting through it. We were unable to observe any other cascade to balance this missing intensity. One possible explanation for this intensity mismatch is the presence of an isomeric state. We searched for an isomeric state by generating time-difference spectra constructed by 189.4, 183.7, and 859.8 keV transitions above 17^+ state as "start" and 273.8, 907.2, and 1495.1 keV transitions below the 17^+ state as "stop" signal. These spectra showed an exponential decay pattern and all of them looked similar, indicating that they were due to the effect of the lifetime of the same level. As statistics in individual spectrum were poor, all these spectra were added (Fig. 9) and from exponential fitting a mean life value of 60(2) ns was extracted.

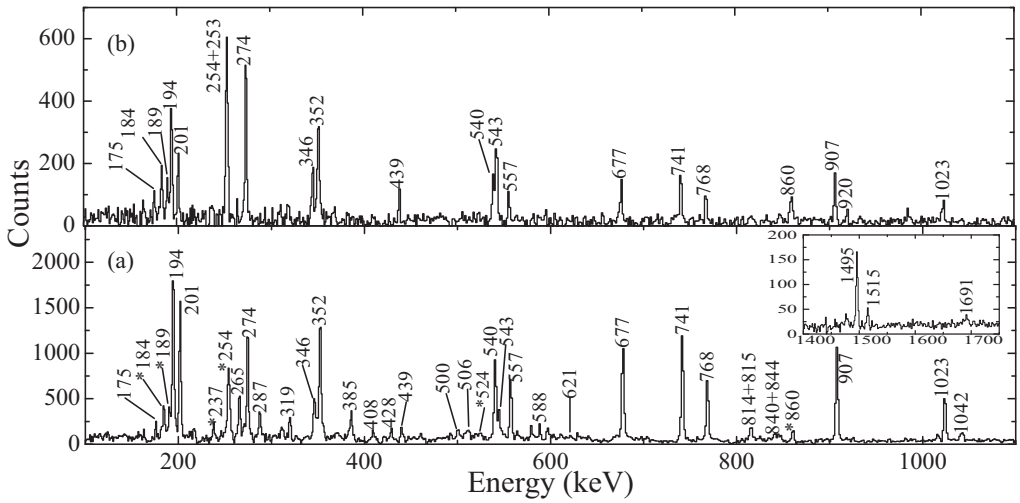

FIG. 7. Representative summed double-gated gamma-ray coincidence spectra show the transitions in ^{142}Sm. The spectra were created with the sum of double-gated spectra of (a) 273.8, 907.2, and 252.9, and (b) 677.1, 193.8, 345.6, 351.8, and 183.7 keV transitions. Peaks marked with asterisks are the transitions above the 17^+ state of structure V in ^{142}Sm.

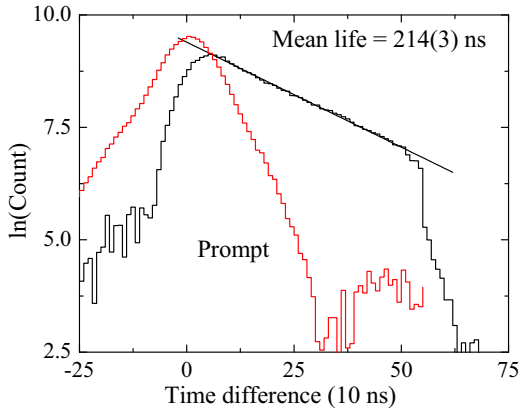

FIG. 8. (Color online) The sum of time-difference spectra was constructed using the 741.1 keV transition as a "start" and any one of the 556.5, 1023.2, and 767.9 keV transitions below the isomeric level as "stop". The prompt was constructed with the coincidence of 1023.2 and 767.9 keV transitions as "start" and "stop" respectively. The solid line, showing the fitting to the selected portion of the experimental spectrum, gives a mean life of 205(4) ns.

The position of the isomer remained uncertain due to the fact that the time-difference spectrum was made by the 254.0 keV transition as the start signal giving full contribution to the prompt coming from the 252.9 keV ($13^- \rightarrow 11^-$) transition, which was a very strong transition.

E. Lineshape analysis

Doppler-broadened line shapes were observed for the dipole transitions of structure IV above the $I^\pi = 16^-$ state and quadrupole transitions of structures I and III above the $I^\pi = 18^+$ and $21^{(-)}$ states, respectively.

The lifetimes of the states were measured using the LINESHAPE analysis codes of Wells and Johnson [42,43]. The

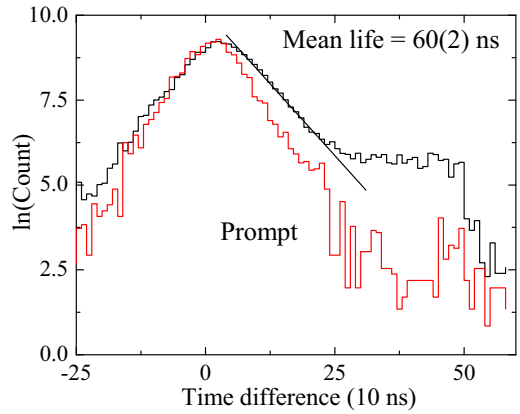

FIG. 9. (Color online) The sum of the time-difference spectra constructed using 189.4, 183.7 and 859.8 keV transitions as a "start" signal and 273.8, 907.2, and 1495.1 keV as "stop" signal. The prompt constructed with the coincidence of 1495.1 and 264.9 keV transitions as "start" and "stop" respectively. The solid line, showing the fitting to the selected portion of the experimental spectrum, gives a mean life of 60(2) ns.

lineshape analysis code was used to generate 10 000 Monte Carlo simulations of the velocity history of the recoiling residual nuclei traversing through the target-backing combination in a time step of 1.5 fs. Shell-corrected tabulations of Northcliffe and Schilling [44] were used to calculate the energy loss of the residual nuclei when interacting with the atomic electrons of the target-backing combination. Velocity profiles for different angles were generated using the geometry of the detectors as well as the array as input parameters. The energies of the gamma transitions and the side-feeding intensities were used as input parameters to obtain the lifetime of the desired state using the LINESHAPE code. In the fitting process, the side-feeding into each level of the band was modeled as a cascade of five transitions having a fixed moment of inertia comparable to that of the investigated band. The topmost transition of the investigated band whose shape was possible to observe in experimental spectra, was assumed to have a 100% side-feeding intensity. The background and stopped peak parameters, corresponding to the best fit for which χ^2 minimization of the simulated lineshape fitted to the experimental spectra occurred, was fixed. Thus, the effective lifetime of the top level was worked out. This procedure of obtaining χ^2 minimization was followed for the next lower levels and after obtaining minimization for each level a global fitting was carried out with fixed window parameters (background and contamination peaks). The forward, transverse, and backward spectra were fitted simultaneously to obtain the level lifetime.

In band IV (henceforth we are referring structures as bands), lineshapes were observed for the 286.7, 385.2, 499.6, 621.4, and 408.0 keV gamma transitions above the 16^- state. For bands I and III, Doppler-broadened lineshapes were observed for the 578.9, 840.0, and 1078.0 keV gamma transitions above the 18^+ state and the 815.4, 923.8 keV transitions above the $23^{(-)}$ state, respectively. For the LINESHAPE analysis, angle-dependent E_γ-E_γ asymmetric matrices were used to construct the background subtracted coincidence spectra at various angles. The gates were set on a transition below the band of interest along the axis of all detectors. For bands I, III, and IV, the forward 65°, 90°, and backward 140° spectra for each transition were fitted simultaneously. From these angle-dependent matrices we were unable to observe the shape of the transitions above the 1078.0 keV (band I), 923.8 keV (band III), and 408.0 keV (band IV) transitions due to lack of statistics. The results of the lifetime analysis are tabulated in Tables III and IV and lineshape fits for the transitions have been presented in Figs. 10 and 11. Uncertainties in the lifetimes were derived from the behavior of the χ^2 fit in the vicinity of the minimum. The effect of variation in the side-feeding intensity resulted in a change in the level lifetime by less than 15%. The experimental transition strength $B(M1)$ (assuming stretched $M1$ transition) and $B(E2)$ values were obtained from the measured lifetimes using the following relationships [45]:

$$B(M1) = \frac{0.05697 B_r\,(M1)}{E_\gamma^3\,(M1)\,\tau[1+\alpha_t\,(M1)]} \quad \text{in } \mu_N^2,$$

$$B(E2) = \frac{0.0816 B_r\,(E2)}{E_\gamma^5\,(E2)\,\tau[1+\alpha_t\,(E2)]} \quad \text{in } (e\text{b})^2,$$

TABLE III. Measured level lifetimes and corresponding $B(M1)$ values for dipole band IV in ^{142}Sm. The quoted uncertainties include the fitting and side-feeding errors but do not include the systematic errors due to the stopping power that can be as large as 15%.

I_i^π	E_γ (keV)	τ (ps)	$B(M1)\mu_N^2$
Band IV			
17^-	286.7	$1.05^{+0.27}_{-0.21}$	$1.92^{+0.51}_{-0.39}$
18^-	385.2	$0.91^{+0.25}_{-0.22}$	$1.10^{+0.30}_{-0.27}$
19^-	499.6	$0.76^{+0.37}_{-0.26}$	$0.60^{+0.30}_{-0.21}$
20^-	621.4	$1.08^{+0.42}_{-0.26}$	$0.08^{+0.04}_{-0.02}$
21^-	408.0	0.57[a]	1.50[b]

[a]Effective lifetime is obtain assuming 100% side-feeding intensity. Hence it is the upper limit of level lifetime (τ).
[b]Lower limit of the $B(M1)$ value.

TABLE IV. Measured level lifetimes and corresponding $B(E2)$ values for quadrupole bands I and III in ^{142}Sm. The quoted uncertainties include the fitting and side-feeding errors.

I_i^π	E_γ (keV)	τ (ps)	$B(E2)$ in W.u.
Band I			
20^+	578.8	$1.32^{+0.48}_{-0.35}$	194^{+71}_{-52}
22^+	840.0	$0.44^{+0.14}_{-0.10}$	99^{+32}_{-23}
24^+	1078.0	0.45[a]	28[b]
Band III			
$25^{(-)}$	815.0	$0.49^{+0.15}_{-0.11}$	103^{+32}_{-23}
$27^{(-)}$	923.8	0.43[a]	66[b]

[a]Effective lifetime is obtain assuming 100% side-feeding intensity. Hence it is the upper limit of level lifetime (τ).
[b]Lower limit of the $B(E2)$ value.

where B_r and α_t are the branching ratio and the total internal conversion coefficient of the transition, respectively.

V. DISCUSSION

The proposed partial level scheme of ^{142}Sm, as shown in Fig. 3, represents a very irregular and complex structure at low and medium excitation energies. Several band-like structures including one dipole band and three quadrupole bands have been observed at higher excitation energy. At lower excitation energy, the ^{142}Sm nucleus is expected to have a small deformation due to the fact that it has two neutrons and two proton holes outside the ^{146}Gd core. In this work, the low-spin behavior of ^{142}Sm has been understood within the shell model picture. On the other hand, at higher excitation energy different kinds of excitation modes have been observed. In this high excitation energy, nuclear shape may evolve from spherical to prolate, oblate, or triaxial [46] shapes. Intrinsic structures of the dipole band have been investigated in the frame work of the semiclassical shears mechanism with the principal axis cranking (SPAC) model, whereas the quadrupole bands have been interpreted in the light of cranked Nilsson-Strutinsky

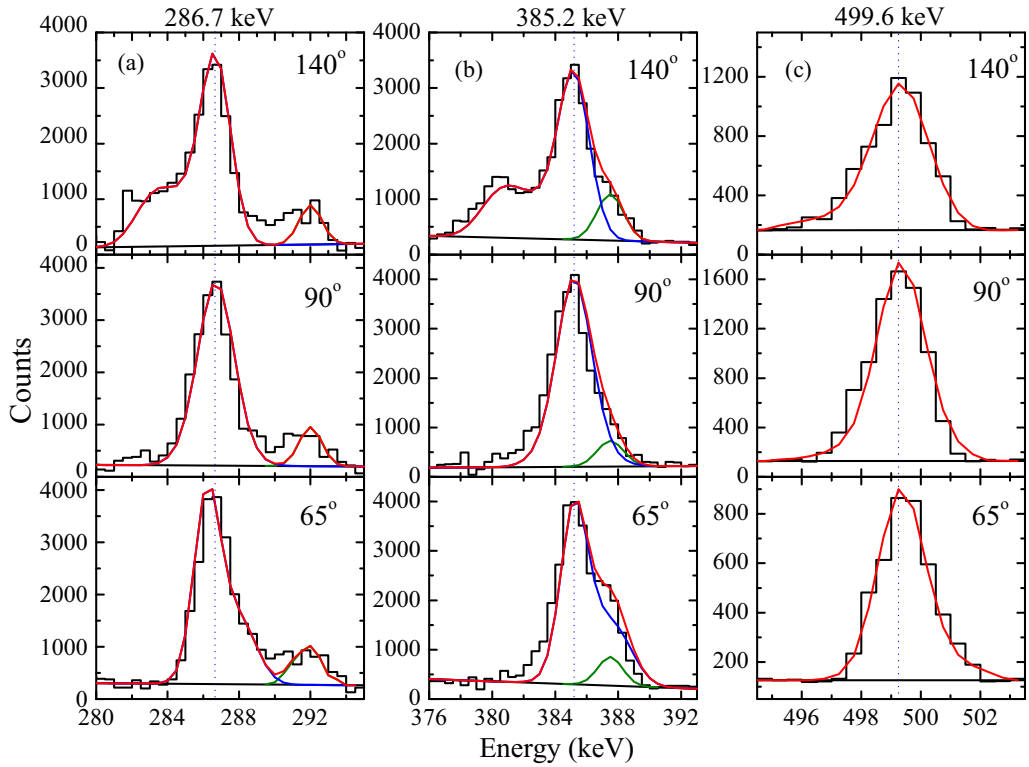

FIG. 10. (Color online) Representative spectra along with theoretically fitted lineshapes for (a) 286.7 keV, (b) 385.2 keV, and (c) 499.6 keV dipole transitions in dipole band IV of ^{142}Sm. The top, middle, and bottom rows correspond to the shapes in the 140°, 90°, and 65° detectors, respectively. The desired lineshapes of gamma transitions, contaminant peaks, and total lineshapes are represented by the blue, olive, and red curves, respectively. The vertical dotted lines represent the stopped peak position for each transition whose shape is observed.

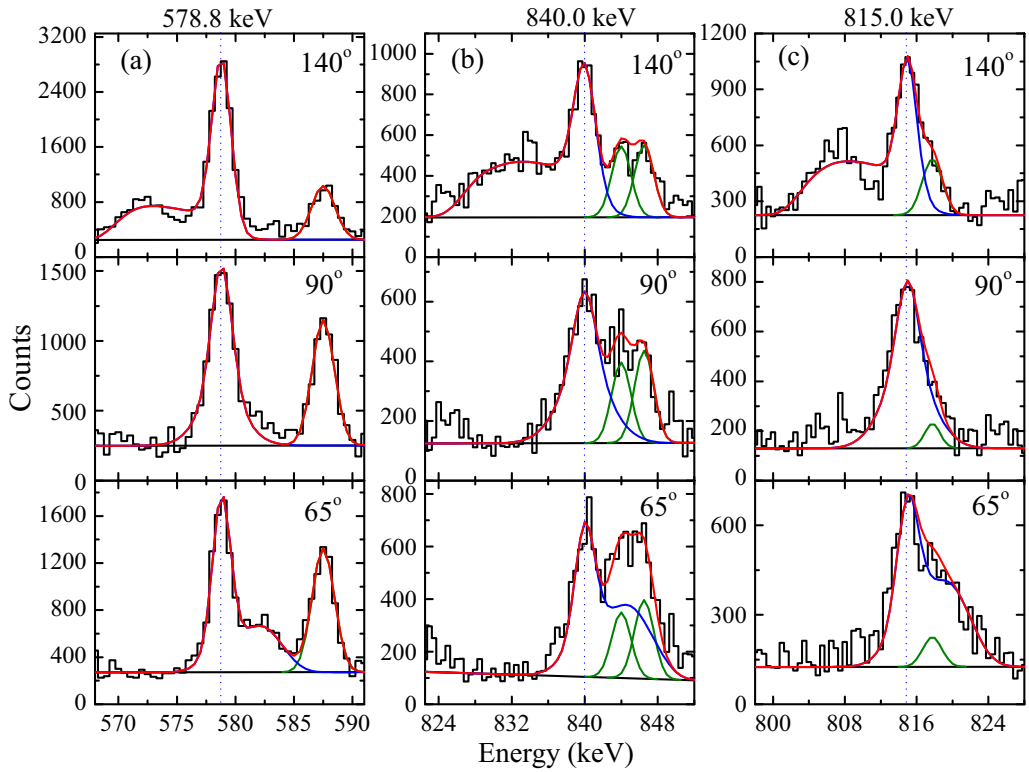

FIG. 11. (Color online) Representative spectra along with theoretically fitted lineshapes for the quadrupole transitions (a) 578.8 and (b) 840.0 keV in the quadrupole band I and (c) 815.0 keV in the quadrupole band III of ^{142}Sm. The top, middle, and bottom rows correspond to the shapes in the 140°, 90°, and 65° detectors, respectively. The desired lineshapes of gamma transitions, contaminant peaks, and total lineshapes are represented by the blue, olive, and red curves, respectively. The vertical dotted lines represent the stopped peak position for each transition whose shape is observed.

(CNS) calculations, exploring the associated shape evolution and/or coexistence in ^{142}Sm.

A. Shell model calculation for low-lying states in ^{142}Sm

Low-lying energy levels were studied using the nuclear shell model code ANTOINE [47–49] up to an excitation energy ≈5.7 MeV and spin-parity 14^+. The 50–82 shells were used for both protons and neutrons. As the dimensions of the matrices were too large, the proton valence space was truncated by allowing only three particles above the $g_{7/2}$ and $d_{5/2}$ levels (as $Z = 64$ is known to be a semishell closure), i.e., in $d_{3/2}$, $s_{1/2}$, and $h_{11/2}$ levels. Although we used the Bonn-A interaction [50], the truncation of the model space necessitated renormalization of the single-particle energy levels and the two-body matrix elements because these were determined for a full shell calculation. The Bonn-A interaction obeys isospin symmetry. The energy levels used in the present calculation, for both protons and neutrons, were as follows: $E(g_{7/2}) =$ 0.1 MeV, $E(d_{5/2}) = 0.4$ MeV, $E(d_{3/2}) = 1.64$ MeV, $E(s_{1/2}) =$ 1.55 MeV, and $E(h_{11/2}) = 0.4$ MeV. Essentially, we changed the energy levels of the $d_{5/2}$ and $h_{11/2}$ orbits. Furthermore, to account for the truncation, all the two-body matrix elements were multiplied by a factor of 1.25. Figure 12 shows the comparison between the calculated and the experimental levels in ^{142}Sm.

Clearly, the calculated lowest 3^- state does not match with its observed counterpart. This is due to the fact that the observed 3^- state is an octupole vibration state, which involves excitation from the core. Additionally, a better agreement, particularly for negative energy states, may be obtained by relaxing the restriction that the proton and the neutron single particle states, particularly the $h_{11/2}$ levels, have the same energy value. Obviously, a less severe truncation will also improve the theoretical results. For example, a calculation allowing four protons in the $h_{11/2}$, $d_{3/2}$, and $s_{1/2}$ orbits reproduced the spacing between lowest 8^+ and 10^+ states very accurately. However, we believe that the present calculation, though restricted in nature, is adequate for our purpose of studying the origin of the observed low-lying states.

The negative parity states up to spin-parity 7^- may predominantly be assigned two quasineutron configuations from the present shell model calculation. The 7^- isomeric state has the fully aligned two-quasiparticle configuration $(\nu h_{11/2}^{-1} \nu d_{3/2}^{-1})$. The existence of this 7^- isomeric state was well established for $N = 80$ isotones in the 140 mass region and has been interpreted from systematics [51] to have the same configuration as obtained from the present calculation. The other states, such as 4^- and 5^-, also have a two-neutron configuration with one quasihole in the $\nu h_{11/2}$ state.

The negative parity levels with spin-parity 8^- to 14^- are observed to be four-quasiparticle states with two proton quasiparticles and two neutron quasiholes. The neutron

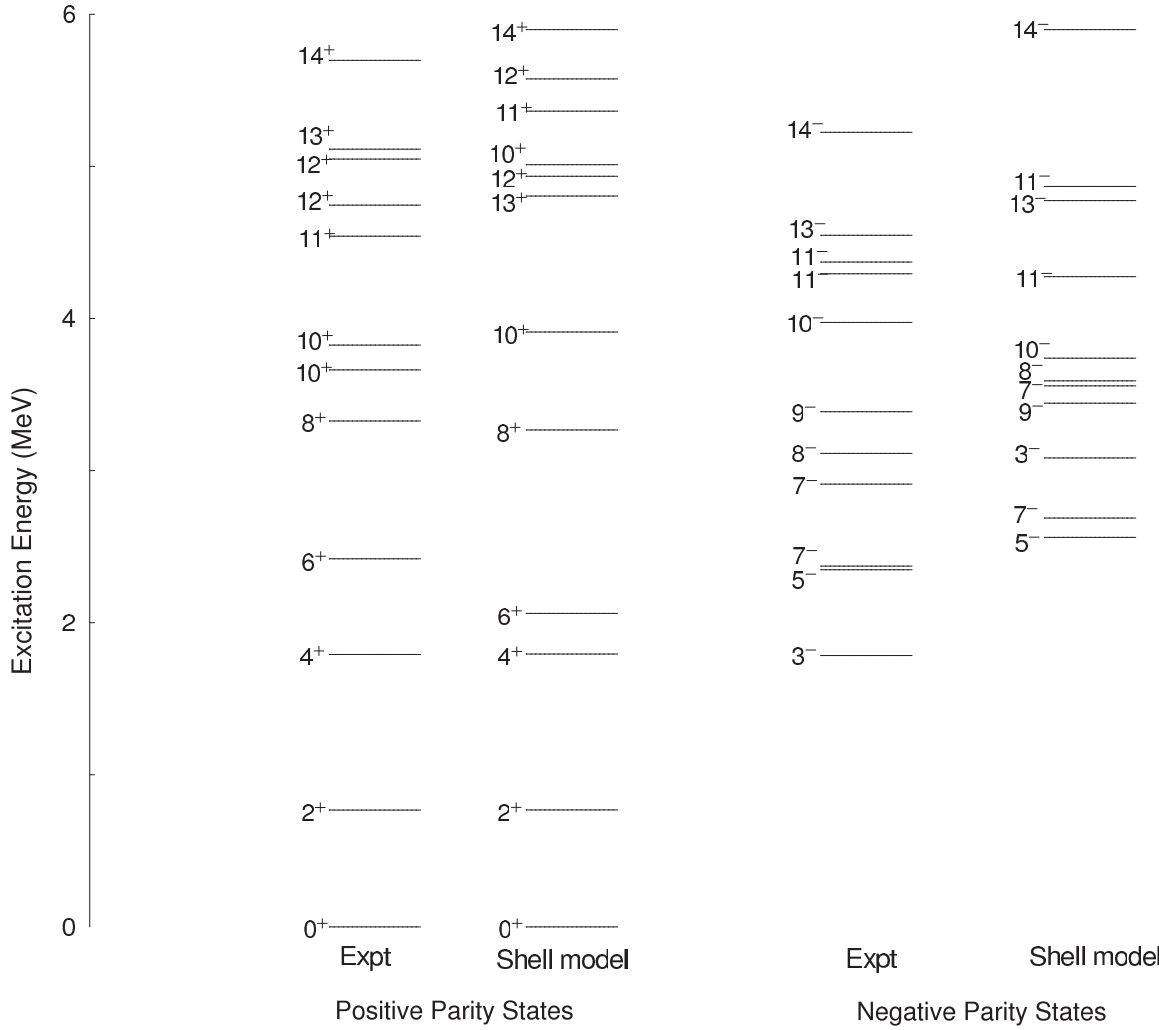

FIG. 12. Comparison between experimental and shell model predicted levels in ^{142}Sm.

configuration is predominantly $(\nu h_{11/2}^{-1}\nu d_{3/2}^{-1})$ while the proton configuration involves one quasihole in the $Z = 64$ core and one particle in either of the $d_{3/2}$ or the $s_{1/2}$ orbits. The only exception is the level 9^-, which is predominantly a two-quasihole state with the configuration $(\nu h_{11/2}^{-1}\nu g_{7/2}^{-1})$.

The lowest positive parity excited states are basically two-quasiparticle states with the dominant contribution coming from the two-quasiproton configuration. The 6^+ state has the predominant quasiparticle configuration $(\pi g_{7/2}^{-1}\pi d_{5/2}^{-1})$. The lowest 8^+ state is a four-quasiarticle state involving two quasiholes in the $Z = 64$ core and two neutron holes in $\nu d_{3/2}$ and $\nu s_{1/2}$ orbits.

The presence of two 10^+ states in the transitional nuclei in this mass region were well studied and their configuration firmly established from systematics as $\nu h_{11/2}^{-2}$ and $\pi h_{11/2}^{2}$. In the case of ^{142}Sm, two 10^+ states are separated only by 163.9 keV in energy with the lower 10^+ state being isomeric, having a mean life of 480 ns. From the present shell model calculation, the configuration of the isomeric 10^+ state has been assigned as $\nu h_{11/2}^{-2}$. The second 10^+ state in our calculation is essentially a four-quasiparticle state. However, possibly because of the severe truncation, the energy has been poorly reproduced. All the higher positive parity states shown in Fig. 12 are four-quasiparticle states.

B. Interpretation of dipole band IV in the light of the SPAC model

A sequence of dipole transitions with regular energy spacing was observed up to $I^\pi = 22^{(-)}$ starting from $I^\pi = 16^-$. Similar dipole bands had been observed in the neighboring nuclei ^{139}Sm, ^{141}Eu, and ^{142}Gd. From their characteristic decrease of $B(M1)$ values with spin [7–10] they had been identified as magnetic rotational bands. The $B(M1)$ values, evaluated for the transitions of band IV, are comparable to those for the dipole bands in ^{139}Sm, ^{141}Eu, and ^{142}Gd [7–10] and the values have also been found to decrease with increase in excitation energy and spin (Table III). This characteristic decrease of $B(M1)$ values (Fig. 14) may be attributed to the fact that these dipole transitions have originated from the shears mechanism. The sudden increase of $B(M1)$ values (at a spin-parity of 21^- in the present case) has already been observed in a different mass region [52–55] in the case of a MR band and interpreted as a crossing of two bands. This will be discussed in the light of theoretical calculations.

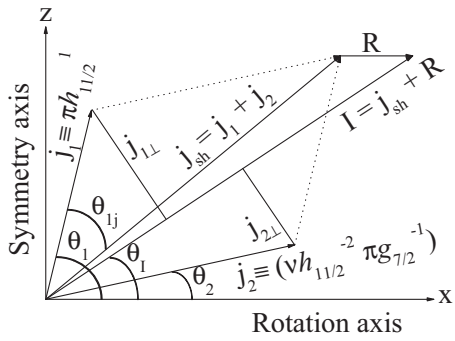

FIG. 13. Schematic description of the angular momentum coupling scheme used in the semiclassical SPAC model calculation and the orientation of shears blades j_1 and j_2 for normal alignment of the dipole band IV in ^{142}Sm.

Calculations have been carried out in the framework of a semiclassical model, called the shears mechanism with principal axis cranking (SPAC) model, in which a part of the core angular momentum ($\vec{R}$) is coupled to the shears angular momentum ($\vec{j_{sh}}$) to generate angular momentum I of the observed states [7–10] (Fig. 13). In this model the total energy of an excited state with spin I can be expressed as

$$E(I) = E(\text{core}) + E(\text{shears}) + \text{const.}$$

Here,

$$E(\text{core}) = \frac{R^2\,(I,\theta_1,\theta_2)}{2J(I)},$$

represents the contribution of the core to the energy $E(I)$, and

$$E(\text{shears}) = v_2 P_2[\cos(\theta_1 - \theta_2)]$$

is the interaction energy due to the shear blades $\vec{j_1}$ and $\vec{j_2}$, where

$$R = \sqrt{I^2 - (j_1 \sin\theta_1 + j_2 \sin\theta_2)^2} - j_1 \cos\theta_1 - j_2 \cos\theta_2.$$

Here, θ_1 and θ_2 are the angle of $\vec{j_1}$ and $\vec{j_2}$ with respect to rotational axis $\hat{x}$. The collective core rotational angular momentum ($\vec{R}$) and core moment of inertia $J(I)$ are assumed to be I dependent and have been described in the band-crossing region by a Boltzmann or Hill function [56]. The reduced transition probabilities of dipole and quadrupole transitions, with the classical approximation for Clebsch-Gordon coefficients, can be written as

$$B(M1) = \frac{3}{8\pi}[j_1 g_1^* \sin(\theta_1 - \theta_I) - j_2 g_2^* \sin(\theta_I - \theta_2)]^2$$

and

$$B(E2) = \frac{15}{128\pi}[Q_{\text{eff}} \sin^2\theta_{1j} + Q_{\text{coll}} \cos^2\theta_I]^2,$$

respectively, where, $g_1^* = g_1 - g_R$, $g_2^* = g_2 - g_R$ and $g_R = \frac{Z}{A}$. Here, Q_{eff} and Q_{coll} are the quasiparticle and quadrupole moments, respectively. Generally, for each value of I, θ_1 and θ_2 can be found from the energy minimization condition

$$\frac{\partial^2 E(I,\theta_1,\theta_2)}{\partial\theta_1,\partial\theta_2} = 0.$$

Initially, any orientation of $\vec{j_1}$ and $\vec{j_2}$ is possible. The direction of $\vec{j_2}$ is set along rotational axis ($\hat{x}$) for normal initial alignment [8–10] and the two-dimensional energy minimization condition has been transformed to one-dimensional condition as

$$\frac{\partial E(I,\theta_1)}{\partial\theta_1} = 0,$$

which is then used to obtain the θ_1 for an excited state with angular momentum I.

In order to perform the SPAC model calculation for this dipole band IV we propose the configuration of the band as $\pi h_{11/2}^1 \otimes \nu h_{11/2}^{-2} \pi g_{7/2}^{-1}$. Results of the calculation are shown in Fig. 14. Most of the magnetic rotational bands in the mass 140 region are built on small oblate deformation. For oblate deformation, one proton hole in the $g_{7/2}$ orbital, being rotation aligned (low Ω), along with two neutron holes in $h_{11/2}$, produce a total angular momentum of $13.5\hbar$, assuming a stretched configuration of all the angular momenta. On the other hand, in another configuration, one proton particle in the $h_{11/2}$ orbital is promoted by creating a hole in $g_{7/2}$ in the $Z = 64$ closed shell and aligned along the symmetry axis with high Ω. This is almost perpendicular to the total angular momentum of rotation aligned holes. The the total angular momentum of this configuration is $15\hbar$. It is observed that this configuration cannot reproduce both the energies and $B(M1)$ values as shown in Figs. 14(c) and 14(d) (represented by dotted lines), in the framework of the SPAC model, simultaneously. In the case of ^{142}Gd, SPAC model calculations [10] were carried out assuming the unstretched shear blade along the rotational axis.

Thus, energy has been minimized assuming the configuration $\pi h_{11/2}^1 \otimes \nu h_{11/2}^{-2} \pi g_{7/2}^{-1}$ for the dipole band II and normal initial alignment with $j_1 = 5.5\hbar$, $g_1 = +1.21$ for proton blades and $j_2 = 11.5\hbar$, $g_2 = -0.014$ for both proton and neutron holes [10]. To reproduce the energy of the states above $I^\pi = 20^-$ a new configuration $\pi h_{11/2}^1 \otimes \nu h_{11/2}^{-2} \pi g_{7/2}^{-3}$ has been proposed. Under these assumptions, energy levels are well reproduced from the one-dimensional minimization condition as shown in Fig. 14(a). Figure 14(a) clearly shows that the shears have reopened after the band crossing at $I^\pi = 21^-$. For initial normal alignment the spin dependences of θ_1, θ_I, and R are shown in Fig. 14(b). The experimental angular momenta are plotted against the rotational frequency ($\hbar\omega$) and the dipole transition strength $B(M1)$ against the spin of the states as shown in Figs. 14(d) and 14(c).

The gradual alignment of two angular momentum blades due to the shear mechanism has resulted in generation of angular momentum along the band up to spin $20\hbar$. The SPAC model calculation show that at this spin the angle between shears is $\sim 11^\circ$ [Fig. 14(a)]. Assuming the same configuration, energy minimization is not achieved for the state at spin $21\hbar$. However, as discussed earlier with the proposed configuration as $\pi h_{11/2}^1 \otimes \nu h_{11/2}^{-2} \pi g_{7/2}^{-3}$ for the shears

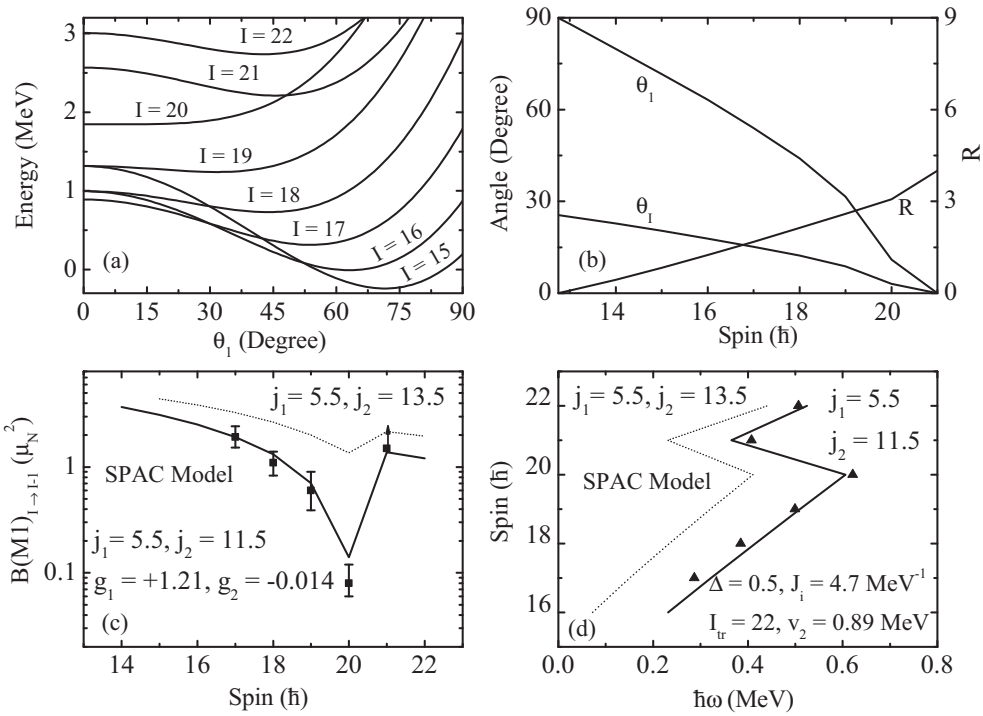

FIG. 14. Comparison of experimental results (represent by full squares) for the dipole band IV in ^{142}Sm in the light of SPAC model (solid lines) calculations. (a) Energy of the excited states as a function of θ_1. (b) Evolution of the angles θ_1, θ_I and collective core rotational angular momentum (R) against spin. (c) $B(M1)$ transition strengths and (d) angular momentum (I) vs $\hbar\omega$ for the dipole band IV are shown. The parameters used for the calculations are given in the figures.

blades, the results of the energy minimization point towards a new shear angle $\sim 45^\circ$. It seems that the shears reopen at this point of crossing of these two configurations. A similar situation has also been observed in ^{199}Pb [54,55] where the original MR band terminates ($\theta_1 = 0$) at a certain frequency after that the shears reopen with a different configuration. The experimental $B(M1)$ values show a characteristics decrease with spin and also back-bending in the I-vs-$\hbar\omega$ plot. The semiclassical SPAC model has reproduced the experimental spin (I) and dipole transition strength $B(M1)$ below and above the band crossing as shown by the solid lines in Figs. 14(d) and 14(c). At spin I_{tr}, a structural change has occurred due to an increase in collectivity, which allows us to explain the back-bending across the band crossing.

C. Interpretation of positive parity quadrupole bands I, II, and III

Above the 18^+ level of the positive parity part of the level scheme, three quadrupole bands have been observed. The value of dynamic moment of inertia ($\approx$20 $\hbar^2$MeV^{-1} for band I) is smaller than those of the observed quadrupole bands in ^{141,142,143,144}Gd [18,19,57–59] and ^{142,143}Eu [32] but similar to those of several such bands observed in the neighboring ^{138,139,140}Nd nuclei, which have been interpreted as triaxially deformed bands [1,60–62].

In this mass region, alignment of nucleons in down-sloping orbitals drives the nucleus towords a well deformed triaxial shape at high spin. Stretched $E2$ cascades with large $B(E2)$ values ($\approx$150 W.u.) have been observed in ^{142,144}Gd and ^{142,143}Eu nuclei in this mass region [11,18,19,32].

In order to understand the intrinsic structure of the observed quadrupole bands in ^{142}Sm, we have carried out calculations in the configuration-dependent cranked Nilsson-Strutinsky (CNS) formalism [63–67] which has already been used to describe the triaxial high-spin rotational bands in ^{138,139,140}Nd [1,60–62]. This model has also successfully explained the high-spin quadrupole bands of nuclei in different regions of the nuclear chart.

In this model, pairing has not been included, and hence results are relevant for description of high-spin excitation. However, reasonable agreement with the observed results in the intermediate-spin regime ($I > 15\hbar$) has been reported for some of the nuclei [68,69]. In this approach, for each major shell $N_{\rm rot}$ of the rotating basis, the singleparticle levels have been grouped into low-j and high-j orbitals. The configurations have been then labeled by the number of particles occupying high-j and a group of low-j orbitals. For ^{142}Sm the following nomenclature has been used for the assignment of configurations:

$$[p_1(p_2), n_1 n_2(n_3 n_4)],$$

where p_1 and p_2 are the numbers of proton particles in $(g_{7/2}d_{5/2})$ and $h_{11/2}$ orbitals, respectively, whereas the numbers of neutrons occupying $(h_{9/2}f_{7/2})$ and $i_{13/2}$ sub-shells have been represented by n_3 and n_4, respectively. Moreover, neutron holes in the $(g_{7/2}d_{5/2})$ and $h_{11/2}$ orbitals have been designated by n_1 and n_2, respectively.

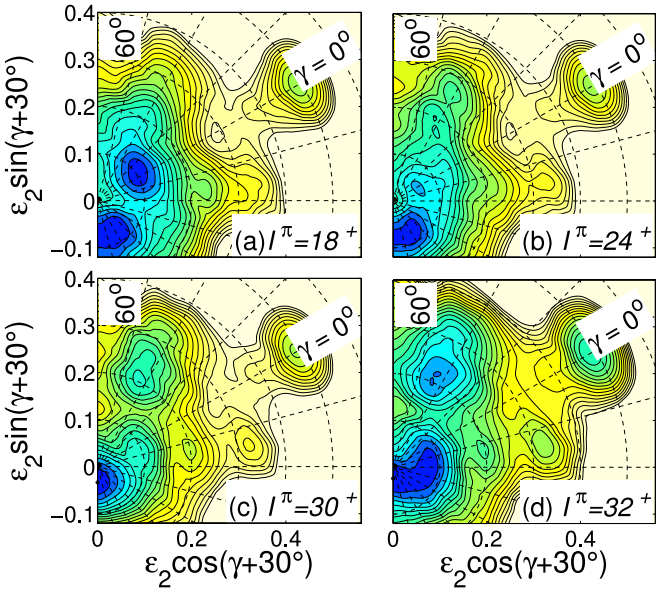

FIG. 15. (Color online) Calculated total energy surfaces for ^{142}Sm at (a) $I = 18\hbar$, (b) $I = 24\hbar$, (c) $I = 30\hbar$, and (d) $I = 32\hbar$ using the configurations ($\pi = +, \alpha = 0$). The contour-line separation is 0.25 MeV.

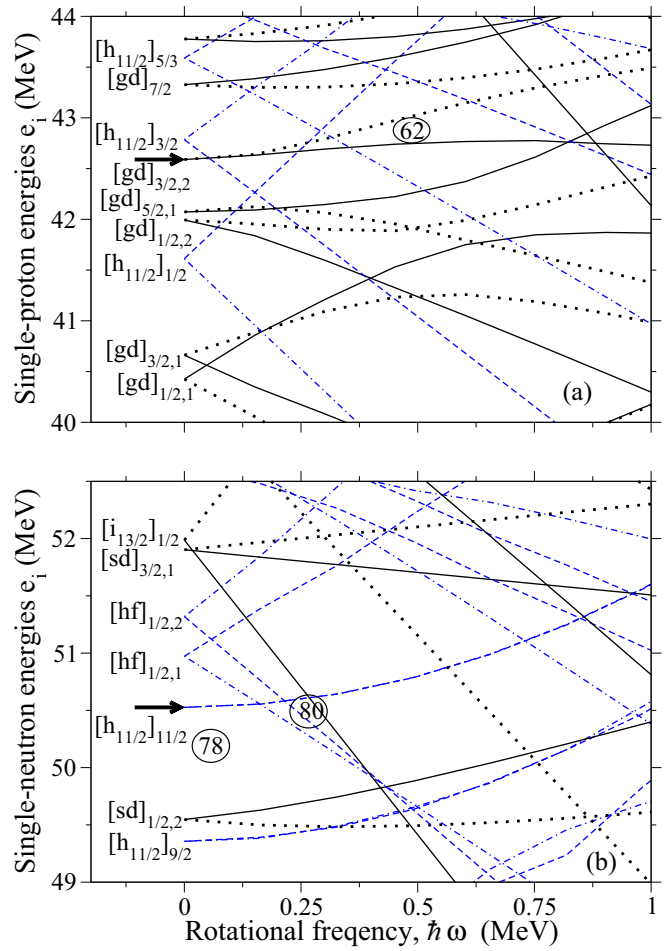

FIG. 16. (Color online) Single-particle (a) proton and (b) neutron energies in a rotating frame as a function of rotational frequency calculated at deformation parameters $\varepsilon_2 = 0.2$, $\varepsilon_4 = 0.008$, and $\gamma \approx 38°$. The four combinations of (π,α) are displayed in the following way: solid lines represent (+, 0) and dotted lines indicate (+, 1), whereas (−, 0) and (−, 1) are represented by dashed and dashed-dotted lines, respectively. The orbitals are labeled for zero rotational frequency. Orbitals with their main amplitudes in the $g_{7/2}d_{5/2}$, $d_{3/2}s_{1/2}$, and $h_{9/2}f_{7/2}$ sub-shells are labeled [gd], [ds], and [hf], respectively, with the ordering and angular momentum projection Ω as subscripts. The two arrows indicate the position of the Fermi level.

In the present calculation the parameters κ and μ, derived for the $A = 150$ region [70], have been employed. These parameters are known to describe the low-deformation configurations in nuclei with a few particles outside the ^{146}Gd core [71]. The Lublin-Strasbourg drop (LSD) model [72] has been used for calculating the microscopic energy, with the rigid-body moments of inertia calculated with a radius parameter of $r_0 = 1.16$ fm and a diffuseness of $a = 0.6$ fm [67]. An energy scale based on mass excess has been applied so that the calculated energies can be directly compared with the observed energy levels. This also allows us to compare high-spin states in nuclei of different masses. The energy of a configuration has been minimized at each spin in a deformation space spanned by the parameters ε_2, ε_4, and γ [63,73].

The calculated potential energy surfaces for ^{142}Sm between the spin range of $I^\pi = 18^+$ to $I^\pi = 24^+$ using the CNS formalism are shown in Fig. 15. Well defined minima are formed at different deformation corresponding to the near-spherical, triaxial, and superdeformed nuclear shapes of ^{142}Sm. The minimum with prolate deformation at $\varepsilon_2 \approx 0.48$ possibly represents a superdeformed structure [74]. This structure becomes yrast at very high spin, beyond the scope of the present work. A triaxial minimum at $\varepsilon_2 \approx 0.20$ and $\gamma \approx 38°$ starts to develop around $I^\pi = 20^+$ and becomes yrast at $I^\pi \approx 32^+$.

Single-particle Routhians for (a) protons and (b) neutrons at the triaxial minimum are shown in Fig. 16. As can be seen from the Routhians (Fig. 16) within the range of observed energies, the lowest configurations involve two or three protons in $h_{11/2}$ orbitals along with a few proton holes in the gd shell. On the other hand, neutrons are excited from the $h_{11/2}$ orbitals to the sharply down-sloping hf and $i_{13/2}$ neutron orbitals.

A search for possible configurations, corresponding to the triaxial minimum at $\varepsilon_2 \approx 0.20$ and $\gamma \approx 38°$, is made involving various possibilities of the numbers of particles in orbitals as well as with the several combinations of parity and signature. Some of the favored configurations which can be assigned to the observed quadrupole bands are shown in Fig. 17(b) where excitation energies relative to the rotating liquid drop energy are plotted as a function of spin. The experimental values are shown in panel (a) of Fig. 17.

The calculated results [Fig. 17(b)] show that the lowest configuration around spin 18$^+$ involves two protons in the $h_{11/2}$ orbital and two neutrons excited to the $(h_{9/2}f_{7/2})$ orbital along with two neutron holes each in the $(d_{3/2}s_{1/2})$ and $h_{11/2}$ orbitals; i.e., in short notation it is [10(2),22(20)]. Therefore, we have assigned the above configuration to band I. A good agreement has been observed between the calculated and experimental

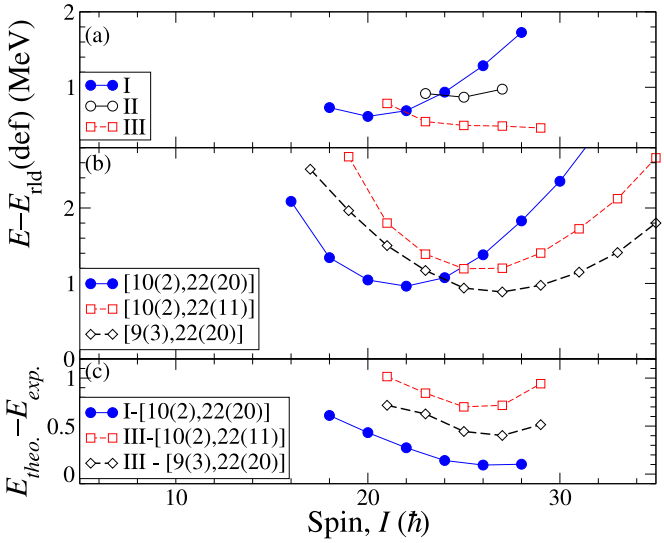

FIG. 17. (Color online) Excitation energies relative to the rotating liquid-drop energy for the (a) observed bands I, II, and III in ^{142}Sm and (b) calculated configurations. The differences between the observed and calculated energies are displayed in panel (c).

energies over the observed spin range, as is evident from the difference plot of Fig. 17(c).

Recently, a large number of bands have been observed in ^{140}Nd [62] in which the quadrupole bands $Q1$, $Q2$, and $Q3$ show decay patterns similar to the quadrupole bands I, II and III in ^{142}Sm, respectively. The calculated [10(2),22(20)] configuration assigned to band I in ^{142}Sm is in agreement with the [8(2),22(20)] configuration of the band $Q1$ in ^{140}Nd [62]. The calculation also predicts a low-lying negative-parity configuration obtained by promoting one of the $(h_{9/2}f_{7/2})$ neutrons of the [10(2),22(20)] configuration to the $i_{13/2}$ orbital; i.e., [10(2),22(11)] and has been assigned to band III. Another configuration, [9(3),22(20)], which involves three protons in the $h_{11/2}$ orbital and two neutrons excited to the $(h_{9/2}f_{7/2})$ orbital along with two neutron holes each in the $(d_{3/2}s_{1/2})$ and $h_{11/2}$ subshells, may also be assigned to band III as it is energetically more favorable than the configuration [10(2),22(11)] (Fig. 17).

The potential energy surfaces for the [10(2),22(20)] and [10(2),22(11)] configurations are shown in Fig. 18. We are unable to find a suitable configuration for band II and hence no configuration has been assigned to the quadrupole band II.

The experimental $B(E2)$ values of the observed quadrupole bands I and III are compared with those calculated for triaxial minima of total potential energy surfaces are shown in Fig. 19. Qualitative agreement between them is an indication of triaxial behavior of the quadrupole bands (band I and III) in ^{142}Sm.

Hence, the quadrupole bands I and III have been produced by promoting two neutrons from the $g_{7/2}d_{5/2}$ orbital to the shape driving intruder orbitals ($h_{9/2}f_{7/2}$ and $i_{13/2}$) which results in the drastic change of nuclear shape from near spherical to triaxial structure. The quadrupole bands arising due to such configurations were interpreted as triaxial bands with rotation around the shortest principle axis ($\gamma \approx 20^\circ$) [1,11].

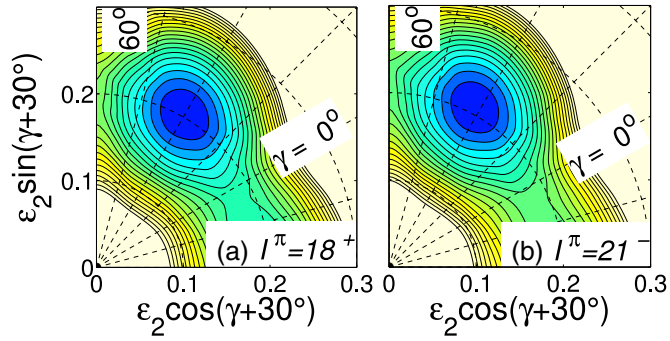

FIG. 18. (Color online) Calculated potential energy surfaces for the configurations (a) [10(2),22(20)] at $I^\pi = 18^+$ and (b) [10(2),22(11)] at $I^\pi = 21^-$; probable band-head spin of the respective observed bands to which the configurations are assigned. The contour-line separation is 0.25 MeV.

VI. SUMMARY

Excited states of ^{142}Sm were investigated through the reaction ^{116}Cd (^{31}P, $p4n$) ^{142}Sm at a beam energy of 148 MeV. The level scheme of ^{142}Sm was extended up to an excitation energy ≈12.5 MeV and spin 28$\hbar$. A new dipole band and three new quadrupole bands were observed in ^{142}Sm. Measurements such as $R_{\rm DCO}$, R_θ, and polarization were performed to determine the electromagnetic properties of the gamma transitions. Lifetimes of five levels of the dipole band IV and five excited of the quadrupole bands I and III were determined by means of DSAM analysis. The experimental $B(M1)$ values of the dipole band IV have been well reproduced in the framework of the shears with principle axis cranking (SPAC) model calculation when small collective core contribution has been assumed. The configurations $\pi h^1_{11/2} \otimes \nu h^{-2}_{11/2}\pi g^{-1}_{7/2}$ and $\pi h^1_{11/2} \otimes \nu h^{-2}_{11/2}\pi g^{-3}_{7/2}$ have been proposed before and after the crossing, respectively, from the SPAC model calculation for the dipole band IV. Experimental $B(M1)$ values as well as rotational frequencies ($\hbar\omega$) have been reproduced well

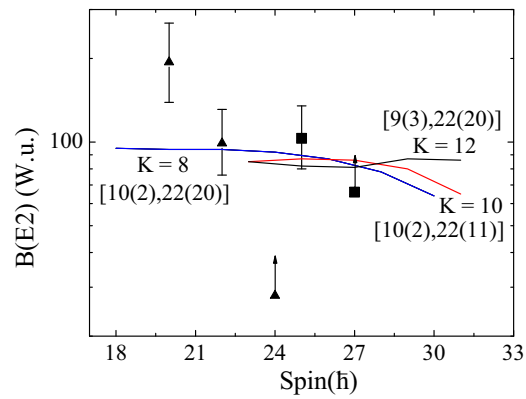

FIG. 19. (Color online) Experimentally observed $B(E2)$ values for quadrupole bands I (filled triangles) and III (filled squarse) of ^{142}Sm. The theoretical (CNS) $B(E2)$ values are calculated using the relation given in Ref. [75], represented by the blue, red, and black lines for the corresponding configurations.

assuming that the hole pairs are initially not fully stretched. Therefore, the dipole band IV in ^{142}Sm has been interpreted as a magnetic rotational band.

The intrinsic structures of the quadrupole bands I and III have been interpreted in the light of the configuration-dependent cranked Nilsson-Strutinsky (CNS) calculation. This calculation indicates that the neutron particles from the core ($g_{7/2}d_{5/2}$ orbital) go to the shape driving $h_{9/2}f_{7/2}$ and $i_{13/2}$ intruder orbitals and produce the observed quadrupole bands (band I and band III) having triaxial origin with $\varepsilon_2 \approx 0.20$ and $\gamma \approx 38^\circ$. The measured quadrupole transition probabilities, i.e., $B(E2)$ values for the states in band I and band III are consistent with the interpretation of the CNS formalism.

ACKNOWLEDGMENTS

The authors would like to acknowledge all INGA collaborators for their sincere help and cooperation. We are sincerely thankful to the Pelletron staff for giving us a steady and uninterrupted ^{31}P beam. The authors would like to thank Professor I. Ragnarsson for helpful discussion and suggestions during the cranked Nilsson-Strutinsky (CNS) calculation. S.R. would like to acknowledge financial assistance form the Council of Scientific and Industrial Research (CSIR), Government of India under Contract No. 09/489(0083)/2010-EMR-1. A.B. (Contract No. 09/489(0068)/2009-EMR-1) and S.N. (Contract No. 09/081(0704)/2009- EMR-I) also would like to acknowledge CSIR for finanacial support. G.G. acknowledges the support provided by the UGC-DRS Programme.

[1] C. M. Petrache *et al.*, Phys. Rev. C **72**, 064318 (2005).
[2] C. M. Petrache *et al.*, At. Data Nucl. Data Tables **59**, 185 (1995).
[3] R. Broda *et al.*, Z. Phys. A **321**, 287 (1985).
[4] N. Redon *et al.*, Z. Phys. A **325**, 127 (1986).
[5] J. Pedersen *et al.*, Phys. Rev. Lett. **39**, 990 (1977).
[6] C. M. Petrache *et al.*, Phys. Rev. C **61**, 011305(R) (1999).
[7] F. Barndolini *et al.*, Phys. Lett. B **388**, 468 (1996).
[8] A. A. Pasternak, E. O. Lieder1, R. M. Lieder, S. Chmel, W. Gast, Ts. Venkova, G. de Angelis, D. R. Napoli, A. Gadea, D. Bazzacco, R. Menegazzo, S. Lunardi, and G. Duchêne, Eur. Phys. J. A **37**, 279 (2008).
[9] E. O. Podsvirova *et al.*, Eur. Phys. J. A **21**, 1 (2004).
[10] A. A. Pasternak *et al.*, Eur. Phys. J. A **23**, 191 (2005).
[11] B. G. Carlsson, I. Ragnarsson, R. Bengtsson, E. O. Lieder, R. M. Lieder, and A. A. Pasternak, Phys. Rev. C **78**, 034316 (2008).
[12] S. Lunardi *et al.*, Phys. Rev. C **42**, 174 (1990).
[13] M. A. Cardona, G. de Angelis, D. Bazzacco, M. De Poli, and S. Lunardi, Z. Phys. A **340**, 345 (1991).
[14] M. Lach, P. Kleinheinz, J. Blomqvist, A. Ercan, H. J. Haihn, D. Wahner, R. Julin, M. Zupancic, F. Cigoroglu, and G. de Angelis, Z. Phys. A **345**, 427 (1993).
[15] R. Raut *et al.*, Phys. Rev. C **73**, 044305 (2006).
[16] S. Frauendorf, Nucl. Phys. A **557**, 259c (1993).
[17] S. Frauendorf, Nucl. Phys. A **677**, 115 (2000).
[18] E. O. Lieder *et al.*, Eur. Phys. J. A **35**, 135 (2008).
[19] R. M. Lieder, A. A. Pasternak, E. O. Podsvirova, A. D. Efimov, V. M. Mikhajlov, R. Wyss, Ts. Venkova, W. Gast, H. M. J. ger, L. Mihailescu, D. Bazzacco, S. Lunardi, R. Menegazzo, C. Rossi Alvarez, G. de Angelis, D. R. Napoli, T. Rzaca-Urban, W. Urban, and A. Dewald, Eur. Phys. J. A **21**, 37 (2004).
[20] M. Lach *et al.*, Z. Phys. A **319**, 235 (1984).
[21] H. Tan *et al.*, in *Nuclear Science Symposium Conference Record 2008* (IEEE, Washington, DC, 2008), p. 3196.
[22] R. Palit, S. Saha, J. Sethi, T. Trivedi, S. Sharma, B. S. Naidu, S. Jadhav, R. Donthi, P. B. Chavan, H. Tan, and W. Hennig, Nucl. Instrum. Methods A **680**, 90 (2012).
[23] R. K. Bhowmik, INGASORT manual (private communication).
[24] D. C. Radford, Nucl. Instrum. Methods, Phys. Res., Sect. A **361**, 297 (1995).
[25] D. C. Radford, Nucl. Instrum. Methods, Phys. Res., Sect. A **361**, 306 (1995).
[26] F. A. Beck, Ann. Phys. (Paris) **1**, 503 (1966).
[27] P. J. Twin, in *The Electromagnetic Inter- action in Nuclear Spectroscopy*, edited by W. D. Hamilton (North-Holland, Amsterdam, 1975), p. 701.
[28] A. Krämer-flecken, T. Morek, R. M. Lieder, W. Gast, G. Hebbinghaus, H. M. Jäger, and W. Urban, Nucl. Instrum. Methods. Phys. Res. A **275**, 333 (1989).
[29] M. K. Kabadiyski, K. P. Lieb, and D. Rudolph, Nucl. Phys. A **563**, 301 (1993).
[30] K. S. Krane, R. M. Steepen, and R. M. Wheeler, Nucl. Data Tables **11**, 351 (1973).
[31] E. S. Macias, W. D. Ruhter, D. C. Camp, and R. G. Lanier, Comput. Phys. Commun. **11**, 75 (1976).
[32] M. Piiparinen, A. Atac, J. Blomqvist, G. B. Hagemann, B. Herskind, R. Julin, S. Juutinen, A. Lampinen, J. Nyberg, G. Sletten, P. Tikkanen, S. Tormanen, A. Virtanen, and R. Wyss, Nucl. Phys. A **605**, 191 (1996).
[33] K. Starosta, T. Morek, Ch. Droste, S. G. Rohozinski, J. Srebrny, A. Wierzchucka, M. Bergstrom, B. Herskind, E. Melby, T. Czosnyka, and P. J. Napiorkowski, Nucl. Instrum. Methods Phys. Res. A **423**, 16 (1999).
[34] Ch. Droste, S. G. Rohoziiiski, K. Starosta, T. Morek. J. Srebrny, and P. Magierskib, Nucl. Instrum. Methods Phys. Res. A **378**, 518 (1996).
[35] J. K. Deng, W. C. Ma, J. H. Hamilton, A. V. Ramayya, J. Rikovska, N. J. Stone, W. L. Croft, R. B. Piercey, J. C. Morgan and P. F. Mantica, Jr., Nucl. Instrum. Methods Phys. Res. A **317**, 242 (1992).
[36] P. M. Jones, L. Wei, F. A. Beck, P. A. Butler, T. Byrski, G. Duchne, G. de France, F. Hannachi, G. D. Jones, and B. Kharraja, Nucl. Instrum. Methods Phys. Res. A **362**, 556 (1995).
[37] R. Palit, H. C. Jain, P. K. Joshi, S. Nagaraj, B. V. T. Rao, S. N. Chintalapudi, and S. S. Ghugre, Pramana **54**, 347 (2000).
[38] O. Klein and Y. Nishina, Z. Phys. **52**, 853 (1929).
[39] N. Xu, C. W. Beausang, J. R. Hughes, Y. Liang, R. Ma, E. S. Paul, W. F. Piel, Jr., S. Shi, and D. B. Fossan, Phys. Rev. C **43**, 2189 (1991).
[40] R. Aryaeinejad, R. B. Firestone, W. H. Bentley, and Wm. C. McHarris, Phys. Rev. C **23**, 194 (1981).

[41] G. G. Kennedy, S. C. Guj rathi, and S. K. Mark, Phys. Rev. C **12**, 553 (1975).
[42] J. C. Wells and N. R. Johnson, Oak Ridge National Laboratory Report No. ORNL-6689, 1991 (unpublished), p. 44.
[43] N. R. Johnson, J. C. Wells, Y. Akovali, C. Baktash, R. Bengtsson, M. J. Brinkman, D. M. Cullen, C. J. Gross, H.-Q. Jin, I.-Y. Lee, A. O. Macchiavelli, F. K. McGowan, W. T. Milner, and C.-H. Yu, Phys. Rev. C **55**, 652 (1997).
[44] L. C. Northcliffe and R. F. Schilling, Nucl. Data Tables A **7**, 233 (1970).
[45] H. Ejiri and M. J. A. de Voigt, *Gamma-Ray and Electron Spectroscopy in Nuclear Physics* (Clarendon, Oxford, 1989), Chap. 6.
[46] S. Frauendorf, Rev. Mod. Phys. **73**, 463 (2001).
[47] E. Caurier, 1999 shell model code ANTOINE, IRES, Strasbourg, 1989–2004 (unpublished).
[48] E. Caurier and F. Nowacki, Acta Phys. Pol. **30**, 705 (1999).
[49] E. Caurier, G. Martinez-Pinedo, F. Nowacki, A. Poves, and A. P. Zuker, Rev. Mod. Phys. **77**, 427 (2005).
[50] R. Machleidt, Adv. Nucl. Phys. **19**, 189 (1989).
[51] M. A. J. Mariscotti *et al*., Nucl. Phys. A **311**, 395 (1978).
[52] Santosh Roy *et al*., Phys. Rev. C **81**, 054311 (2010).
[53] J. R. Cooper, R. Krücken, C. W. Beausang, J. R. Novak, A. Dewald, T. Klug, G. Kemper, P. von Brentano, M. P. Carpenter, R. V. F. Janssens, C. J. Lister, and I. Wiedenhöver, Phys. Rev. Lett. **87**, 132503 (2001).
[54] R. M. Clark, S. J. Asztalos, G. Baldsiefen, J. A. Becker, L. Bernstein, M. A. Deleplanque, R. M. Diamond, P. Fallon, I. M. Hibbert, H. Hübel, R. Krücken, I. Y. Lee, A. O. Macchiavelli, R. W. MacLeod, G. Schmid, F. S. Stephens, K. Vetter, R. Wadsworth, and S. Frauendorf, Phys. Rev. Lett. **78**, 1868 (1997).
[55] M. Neffgen *et al*., Nucl. Phys. A **595**, 499 (1995).
[56] A. A. Pasternak, E. O. Liedera, and R. M. Liederb, Acta Phys. Pol. B **40**, 647 (2009).
[57] S. M. Mullins *et al*., Phys. Rev. C **47**, R2447 (1993).
[58] M. Sugawara, H. Kusakari, Y. Igari, K. Myojin, D. Nishimiya, S. Mitarai, M. Oshima, T. Hayakawa, M. Kidera, K. Furutaka, and Y. Hatsukawa, Eur. Phys. J. A **1**, 123 (1998).
[59] T. Rzaca-Urban *et al*., Nucl. Phys. A **579**, 319 (1994).
[60] C. M. Petrache, S. Frauendorf, M. Matsuzaki, R. Leguillon, T. Zerrouki, S. Lunardi, D. Bazzacco, C. A. Ur, E. Farnea, C. Rossi Alvarez, R. Venturelli, and G. de Angelis, Phys. Rev. C **86**, 044321 (2012).
[61] S. Bhowal *et al*., Phys. Rev. C **84**, 024313 (2011).
[62] R. Leguillon *et al*., Phys. Rev. C **88**, 014323 (2013).
[63] T. Bengtsson and I. Ragnarsson, Nucl. Phys. A **436**, 14 (1985).
[64] I. Ragnarsson, Phys. Lett. B **264**, 5 (1991).
[65] A. V. Afanasjev and I. Ragnarsson, Nucl. Phys. A **608**, 176 (1996).
[66] A. V. Afanasjev, D. B. Fossan, G. J. Lane, and I. Ragnarsson, Phys. Rep. **322**, 1 (1999).
[67] B. G. Carlsson and I. Ragnarsson, Phys. Rev. C **74**, 011302(R) (2006).
[68] K. Starosta *et al*., Phys. Rev. C **64**, 014304 (2001).
[69] P. Singh *et al*., Phys. Rev. C **82**, 034301 (2010).
[70] T. Bengtsson, Nucl. Phys. A **512**, 124 (1990).
[71] M. Mustafa *et al*., Phys. Rev. C **84**, 054320 (2011), and references therein.
[72] K. Pomorski and J. Dudek, Phys. Rev. C **67**, 044316(R) (2003).
[73] S. G. Rohozinski, Phys. Rev. C **56**, 165 (1997).
[74] A. Neußer *et al*., Phys. Rev. C **70**, 064315 (2004).
[75] A. Juodagalvis, I. Ragnarsson, and S. Aberg, Phys. Lett. B **477**, 66 (2000).